Fundamental Study on Flow Characteristics of Disrupted Core Pool at a Low Energy Level
(Joint Research)

Koji MORITA*, Ping LIU*, Tatsuya MATSUMOTO*
Kenji FUKUDA* Yoshiharu TOBITA and Ikken SATO

Reactor Safety Engineering Group
Advanced Nuclear System Research and Development Directorate

March 2007

Japan Atomic Energy Agency　　日本原子力研究開発機構

JAEA-Research

Fundamental Study on Flow Characteristics of Disrupted Core Pool at a Low Energy Level
(Joint Research)

Koji MORITA*, Ping LIU*, Tatsuya MATSUMOTO*, Kenji FUKUDA*
Yoshiharu TOBITA and Ikken SATO

FBR Safety & Innovative Technology Unit
Advanced Nuclear System Research and Development Directorate
Japan Atomic Energy Agency
O-arai-machi, Higashiibaraki-gun, Ibaraki-ken

Dynamic behaviors of solid particle beds in a liquid pool against pressure transients were investigated to model the mobility of core materials in a low-energy disrupted core of a liquid metal fast reactor. A series of experiments was performed with a particle bed of different heights, comprising different monotype solid particles, where variable initial pressures of the originally pressurized nitrogen gas were adopted as the pressure source. Computational simulations of the experiments were performed using SIMMER-III, a fast reactor safety analysis code. Experimental analyses using the SIMMER-III code show that physical models and methods used in the code can reasonably represent the transient behaviors of multiphase flows with rich solid phase as observed in the experiments. The validation of several key models of SIMMER-III was also discussed for treating transient behaviors of the solid-particle phase in multiphase flows.

低エネルギー炉心プールの流動特性に関する基礎的研究
（共同研究）

日本原子力研究開発機構

次世代原子力システム研究開発部門　FBR システムユニット

守田 幸路*、劉 平*、松元 達也*、福田 研二*、飛田 吉春、佐藤 一憲

　液体金属高速炉の低エネルギー損傷炉心における炉心物質の流動性をモデル化するため、液体プール中における固体粒子層の圧力過渡に対する運動挙動について研究を行った。圧力源として加圧窒素を用い、初期圧力、固体粒子層高さ、固体粒子タイプをパラメータとした一連の実験とともに、高速炉安全解析コード SIMMER-III を用いた数値シミュレーションを実施した。SIMMER-III コードを用いた実験解析の結果は、本コードの物理モデルや手法が実験で観察された固相の割合が高い多相流の過渡挙動を適切に表現できることを示した。多相流における固体粒子相の過渡挙動を取り扱う上で重要な SIMMER-III のモデルの妥当性についても議論した。

Contents

目次

List of Tables and Figures

This is a blank page.

1 Introduction

SIMMER-III[1,2] is a next generation computer program used to predict the coupled neutron and fluid-dynamics behaviors of liquid metal fast reactors (LMFRs) during core disruptive accidents (CDAs). It is a two-dimensional, multi-velocity-field, multiphase, multi-component, Eulerian fluid dynamics code coupled with a fuel-pin model and a space- and energy-dependent neutron kinetics model. In order to model the complex flow phenomena in a postulated disrupted core, the mass and energy conservation equations are solved for 30 density and 17 energy components, respectively. Multi-velocity fields (up to seven for liquids and one for vapor) are modeled to simulate the movement of the different fluid components. The fluid convection is treated using a semi-implicit method.

The development of the SIMMER-III code has successfully reached a milestone with the completion of all of the physical models originally intended for simulating accident sequences of CDAs in LMFRs.[2] It has been applied to many kinds of LMFR safety analyses, which have proved its general validity and flexibility. Meanwhile, in order to apply it more widely and reliably to the accident analysis of any future or advanced fast reactors, the improvement and assessment of SIMMER-III is still an on-going program for general types of multiphase flow problems.

In a CDA of an LMFR, there is a possibility of the formation of a disrupted core, in which solid particle-liquid multiphase flows are formed comprising a mixture of molten fuel, molten structure, refrozen fuel and solid fuel pellets, *etc*. In Fig. 1, a schematic view of this kind of disrupted core is shown. It is anticipated that such multiphase flows with rich solid phases might cause the formation of a degraded core with low mobility. Severe recriticality due to massive relocation of disrupted fuel in the core, which is a matter of great importance to the fast reactor safety, could be prevented in this situation. From a safety assessment point of view, however, it is difficult to consider the low fluidity of a mixture of solid particles and liquid components in the present CDA analysis on a conservative basis. This is because we have insufficient knowledge about the behavior of multiphase flows with rich solid phases in a postulated disrupted core, regardless of its importance to the recriticality event.

In the SIMMER-III code, there are some models that take consideration of the extra influence of solid particles on the behavior of multiphase flows, such as the particle viscosity model[6,7] and the particle jamming model.[4] The particle viscosity model, which is based on equations proposed by Russel,[8] was introduced to model the effective increase in the fluid viscosity of materials due to the existence of solid particles in the molten mixture, while the particle jamming model was used to ensure that the volume fraction of solid particles does not exceed a maximum packing fraction in computational cells. These models were initially introduced to SIMMER-III to consider the effect of solid phases in channel flows. Besides, the viscous diffusion term, i.e. the momentum diffusion term,[9] was implemented for the purpose of investigating the effect of bubbles on the behavior of a molten pool. The particle viscosity model is applied to the fluid viscosity in both the viscous diffusion term as well as the fluid-fluid drag term. Despite the existence of these models, however, little work has been performed with regards to verifying the validity of the SIMMER-III code on simulating the dynamic behaviors of pool multiphase flows with rich solid particles.

On the other hand, concerning multiphase or two-phase flows with rich solid particles, significant advances have been made in numerical modeling during the past few decades, especially in gas-solid flows. For example, Gidaspow and his co-workers worked on a two/multi-fluid approach,[10],[11] while Tsuji and his co-workers[12),13)] concentrated their efforts on establishing a distinct element model. Gera et al.[13] has made a comparison of the two approaches. Generally, the Eulerian-Lagrangian approach is well applied to simulations with a small number of particles, while the Eulerian two/multi-fluid model is a preferred method for simulating the fluid dynamics of highly loaded particle flows.[14),15)] However, while all of the above works are mainly concerned with fluidized beds, the available experiments were performed with small solid particles or fine powders mainly in a two-dimensional column, which may be very different from the pool multiphase phenomena in a postulated disrupted reactor core with relatively larger solid particles mixed with melted fuel *etc*.

Therefore, here we performed a series of experiments to simulate the dynamic behavior of solid particle beds in a liquid pool against pressure transients in order to verify the validity of the SIMMER-III code on describing the behavior of the multiphase flows with rich solid phases.

This report is organized as follows. The experimental methods and conditions are explained in Chapter 2. Simulations models and methods of SIMMER-III, as well as the simulation geometry for the experiments, is described in Chapter 3. Chapter 4 mainly presents results of a sensitivity analysis of models while analysis of all experiments are presented and discussed in Chapter 5. In the last chapter, conclusions are drawn.

2 Pool multiphase flow experiments

2.1 Experimental apparatus and method

A schematic view of the main part of the experimental apparatus including key dimensions are illustrated in Fig. 2 while Fig. 3 is a schematic view of the whole experimental system. The basic apparatus consists mainly of a cylindrical water pool (inner diameter 310 mm and height 1000 mm) constructed from a transparent acrylic resin. Steel flanges are used for connections at both the top and the bottom of the cylindrical water pool. Above the top flange, there is an upper pipe with an inner diameter of 100 mm and a height of 500 mm. In the upper pipe, a floater is set on the water surface to allow the water level change to be easily recorded using a high-speed camera. Beneath the bottom flange, there is a cylindrical pressure vessel (inner diameter of 50 mm) constructed from stainless steel, whose effective capacity is about 560 cm^3 and whose exit is closed with a rupture disk prior to the beginning of each experiment. A container (inner diameter of 290 mm and height of 160 mm) used for holding particles is placed inside the cylindrical pool. Two plates with a total height of 25 mm are installed at the bottom of the container. An iron sieve with a 5.5 mm-aperture and negligible thickness is positioned between the two plates to prevent particles with the diameter of 6 mm from falling down. The plate, which is under the iron sieve, is used to allow the laser beam to pass through for detecting the gas phase evolving from the pressure vessel.

The cylindrical water pool is surrounded by a quadrate water pool (420 mm × 420 mm × 1000 mm) made from transparent acrylic resin, in which water is filled up to 800 mm in height to make visual observation inside the cylinder both possible and reasonable by avoiding the convex effect of the cylinder. Two pressure sensors are installed to measure the pressure transients in the pressure vessel and at the top of the water pool. After the rupture disk breaks, nitrogen gas is ejected from the pressure vessel into the water pool, driving the particle bed upward. At the same time, the pressure transducers shown in Fig. 2 transfer the pressure transient information to a PC-based data acquisition system as shown in Fig. 3. Two high-speed cameras, both of which can record 400 frames per second, are used to record the movements of the particle beds and the water surface level changes in the upper pipe, respectively.

The rupture disk used to seal the pressure vessel at the beginning of the experiment is a hand-made diaphragm of polyester resin, which is designed to rupture at a desired pressure. When the pressure in the pressure vessel reaches the rupture limit of the diaphragm, the rupture disk will break and the initially pressurized nitrogen gas will spurt into the pool, thereby driving the particle bed upward inside the water pool. The water pool is filled with room temperature water up to the upper pipe with a height of around 115 mm from the top of the water pool. As shown in Fig. 3, the pressure vessel is charged with pressurized nitrogen gas directly from a nitrogen bottle and the breaking of the rupture disk is triggered by the release of the pressurized nitrogen gas in the supply line controlled by two valves. The valve on the nitrogen bottle side is closed when the rupture disk breaks and will not be opened thereafter. Therefore, no more gas will be supplied to the pressure vessel from the nitrogen bottle during the expansion process of the nitrogen gas. The laser detector at the bottom of the inner water pool determines the instance when the nitrogen gas is released into the inner water pool, and subsequently a signal is sent out to trigger the two high-speed cameras to begin operating. Figure 3 schematically illustrates the triggering signal - PC - camera system.

2.2 Experimental conditions

In a postulated disrupted core of a sodium-cooled fast reactor, the liquid phase can be sodium coolant, molten fuel or molten steel while possible solid particles may include steel, fuel pellets and refrozen fuel *etc.*, as sketched in Fig. 1. In order to model the behavior of the pool multiphase flows with solid particles much closer to the phenomena, which may happen in a disrupted core, and since room temperature water is used as the experimental liquid phase, different kinds of solid particles, with a density in a range from close to water to that of stainless steel, were used to form the particle bed in the water pool.

The general experimental conditions are shown in Table 1. Four kinds of particles, with the same diameter (6 mm) but different densities were used to form a 50 mm height particle bed within the inner container positioned at the bottom of the water pool. The particles used include plastic particles (YB balls) with a density of 1010 kg/m³, plastic particles of another material (BB balls) with a density of 2210 kg/m³, Al_2O_3 balls with a density of 3580 kg/m³, and stainless steel particles (SS balls) with a density of 7970 kg/m³. The initial particle volume fractions in the particle beds, which were just as they were, were in the range 0.61 - 0.65.

Two kinds of further experiments were performed with a 100 mm height particle bed using SS balls and Al_2O_3 balls, respectively. Moreover, experiments were also performed when Al_2O_3 balls were used to form a 200 mm and a 300 mm height particle bed, respectively, placed at the bottom of a taller inner container compared to the one sketched in Fig. 2. The taller inner container has an inner diameter of 280 mm and a height of 510 mm. Those additional cases were performed to investigate the influence of the particle bed height on the flow behaviors. For each particle bed, bed height and type of solid particle used, experiments were performed with different rupture pressures ranging from around 0.2 to about 0.3 MPa. As a point of reference, experiments were repeated without particle beds using the same experimental setup.

Besides, as that will be explained in Chapter 5, additional experiments with a lower water height in the pool has been performed to check the influence of the water height on the pressure transients in the pressure vessel. In these additional experiments, the distance between the water surface and the top of the water pool is 300 mm.

3   SIMMER-III models and methods

3.1   Multiphase flow models

In the SIMMER-III code, conservation equations are written for independent variables in a unit volume. Therefore, the mass equation is written with respective to macroscopic density, for which formula $\bar{\rho} = \alpha/\upsilon$ is used, where α is the volume fraction and υ is the specific volume.

The experimental conditions described in Chapter 2 indicate that there is no necessary to consider heat and mass transfers, so the experimental three-phase flows of solid particles, water and nitrogen gas, which are, respectively, assigned to different velocity fields, can be modeled by the following three-fluid mass and momentum equations:[1),9)]

$$\frac{\partial \bar{\rho}_q}{\partial t} + \nabla \cdot (\bar{\rho}_q v_q) = 0 \tag{3-1}$$

$$\frac{\partial \bar{\rho}_q v_q}{\partial t} + \nabla \cdot (\bar{\rho}_q v_q v_q)$$

$$= -\alpha_q \nabla p + \bar{\rho}_q g - K_{qs} v_q + \sum_{q'} K_{qq'}(v_{q'} - v_q) + VM_q - \left[\nabla \cdot (2\alpha_q \mu_q S_q) - \nabla(\frac{2}{3}\alpha_q \mu_q (\nabla \cdot v_q)) \right] \tag{3-2}$$

where q and q' (= 1, 2, and 3) represent the components of the three phases, v is the velocity vector, VM_q is the virtual mass term, S_q is the strain rate, K_{qs} and $K_{qq'}$ are called momentum exchange functions, which will be explained later.

The above conservation equations indicate that in the SIMMER-III code with a consideration of 30 density components in 8 velocity fields, all phases are assumed to share the same pressure field, i.e. there is no consideration of the solid-phase pressure and the solid-phase stress tensor, which have been considered by some researchers in the modeling of gas-solid fluidized beds.[10),11),14)–16)]

The overall fluid dynamics solution algorithm of the SIMMER-III code is based on a time-factorization approach called the four-step method developed for AFDM, in which intra-cell interfacial area source terms, momentum exchange functions *etc.* are determined separately from inter-cell fluid convection.[5)]

3.2   Momentum exchange functions and viscous diffusion term

In the momentum Eq. (3-2), the term $K_{qs} v_q$ is the fluid-structure drag while K_{qs} is called the momentum exchange function between velocity component q and structure. In pool flow, the influence of structure could be ignored, the detail description of K_{qs} will not be describe here, but it needs to be pointed out that in the SIMMER-III code, K_{qs} has more functions than the above definition. Pressure drop coefficients are added to K_{qs} in order to consider the pressure drop through an orifice, and the effect of a particle jamming model, which will be explained later, can also be taken into consideration though K_{qs}.

Because both theoretical and experimental knowledge of details is limited for a multi-component

multi-velocity flow, the fluid-fluid drag term $\sum_{q'} K_{qq'}(v_{q'} - v_q)$ of Eq. (3-2) is formed based on an analogy from engineering correlations of the steady-state two-velocity flow. $K_{qq'}$ is called the momentum exchange function between components q and q', among which the $K_{qq'}$ between continuous and discontinuous components are modeled based on Ishii's drag-similarity hypothesis.[17] The mathematical form for $K_{qq'}$ is defined as:

$$K_{qq'} = A_{qq'} + B_{qq'}|v_q - v_{q'}|$$ (3-3)

where $A_{qq'}$ is called the viscous term while $B_{qq'}$ stands for the turbulent term. The quantities $A_{qq'}$ and $B_{qq'}$ are functions of flow regime, volume fraction, velocities, binary contact areas, and viscosities. Detailed definition of $K_{qq'}$ can be referred to the work of Tobita et al. in 1991.[18] In the SIMMER-III code, this fluid-fluid drag term is simulated for the purpose of considering the intra-cell momentum transfer between different velocity components.

The eighth term in the left hand side of Eq. (3-2) is the so-called Viscous Diffusion Term (VDT). In the SIMMER-III code, this term is simulated to represent the inter-cell momentum transfer of velocity component q. The viscous diffusion term was initially introduced to the SIMMER-III code for the investigation of the effect of bubbles on the behavior of a molten pool.[9] So far, however, little verification work has been done about the effect of this term on simulating pool multiphase flows with rich particles. In this report, the effect of this viscous diffusion term coupled with the following particle viscosity model will be discussed.

3.3 Particle viscosity model

In order to simulate the penetration of molten materials into, and their blockage formation in, a cold structure channel during CDAs, it is important to simulate the effective increase of the fluid viscosity of the materials due to the existence of solid particles in the molten mixture. Russel[8] has made a comprehensive report relevant to the viscosity increase due to the solid particles and has proposed the following formulation for colloidal suspensions:

$$\frac{\mu_C}{\mu_L} = \begin{cases} 1 + 2.5\alpha_P + 6.2\alpha_P^2 + O(\alpha_P^3) & \alpha_P \leq 0.3 \\ \dfrac{8}{9}\dfrac{(\alpha_P/\alpha_{MP})^{1/3}}{1-(\alpha_P/\alpha_{MP})^{1/3}} & 0.3 \leq \alpha_P \leq \alpha_{MP} \end{cases}$$ (3-4)

where μ_C is the effective viscosity of the continuous liquid phase, μ_L is the viscosity of the continuous liquid phase, α is the volume fraction, the subscripts L and P stand for liquid and solid particles, respectively, and $\alpha_{MP} = 0.62$ is the maximum volume fraction of solid particles.

The above formulation was verified by experimental data[19],[20] using water and polystyrene latex-particles with a diameter of 0.1 to 1.12×10^{-6} m. The applicability of Eq. (3-4) to systems with much larger particles needs further discussion, but this issue is outside the analysis range of this study.

A particle viscosity model based on Eq. (3-4) was introduced to the SIMMMER-III code by replacing it with the following formulation:[6],[7]

$$\mu_C = \mu_L \left\{ \frac{\alpha_L}{\alpha_L + \alpha_P} + \frac{f\alpha_{MP}\alpha_P}{\alpha_{MP}(\alpha_L + \alpha_P) - \alpha_P} \right\} \tag{3-5}$$

where f is a model parameter. Tailored from Eq. (3-4) proposed by Russel, Eq. (3-5) is used in the SIMMER-III code with $f = 5.0$. This reformatted equation realizes the smooth change of effective viscosity over the wide range of particle volume fraction. Figure 4 shows the comparison of effective viscosity between Eqs. (3-4) and (3-5) as a function of effective volume fraction $\alpha_P/(\alpha_L + \alpha_P)$ of solid particles in the liquid and solid-particle phases.[7] In SIMMER-III calculations, a numerically large constant value is assigned to μ_C/μ_L when $\alpha_P/(\alpha_L + \alpha_P)$ exceeds α_{MP}.

With the application of Eq. (3-5) in SIMMER-III, μ_C is used to substitute the conventional liquid viscosity appearing in the calculation of the quantities $A_{qq'}$ and $B_{qq'}$ as well as μ_q in the viscous diffusion term. Although the particle viscosity model was originally introduced to SIMMER-III in the simulation with respect to the penetration and blockage formation of molten materials to a structure channel, little work has been done toward the verification of its effect on the simulation of pool multiphase flows with rich particles. In this study, the influence of this particle viscosity model on the dynamic behavior of the particle bed in a liquid pool will be considered.

3.4 Particle jamming model

A particle jamming model was also developed in SIMMER-III in order to appropriately simulate the blockage formation of molten materials when penetrating into a structure channel. Considering a situation in which solid particles flow into a cavity and accumulate from the bottom, solid particles usually cannot occupy all of the space in the cavity, and thus their volume fraction has a certain maximum value. This phenomenon is called "particle jamming." As shown by Fig. 5, in SIMMER-III, this is modeled by inhibiting the inflow of solid particles into a computational mesh cell when the volume fraction of solid particle in the cell exceeds a maximum packing fraction by assigning a large value to the momentum exchange function at the cell interface.

The idea behind the particle jamming model is to define a function of the volume fraction of particles, which increase exponentially with the increase of particle volume fraction and become large as the maximum packing fraction is approached in a computational mesh cell. Using the same function[4] adopted by SIMMER-II, a particle jamming function was introduced to the SIMMER-III code. The function is based on the assumption that when the solid particle volume fraction is smaller than a defined maximum packing fraction, the function remains equal to zero, but when the solid particle volume fraction approaches the maximum packing fraction, then the function will rapidly increase to an infinite value. This particle jamming model is expressed by the following formulation:[7]

$$\phi = \max \left\{ 1 - \frac{\max(\alpha_P - \alpha_{PJmax}\beta_{PJ}, 0)}{\alpha_{PJmax}(1 - \beta_{PJ})}, 0.1 \right\}^{C_{PJ}} - 1 \tag{3-6}$$

where $\alpha_{PJmax} = 0.7$ is the maximum volume fraction of solid particles while $\beta_{PJ} = 0.95$ is the fraction of α_{PJmax} above which the particle jamming model is applied. The model parameter C_{PJ} is set to -10.0.

This function remains zero (*i.e.* $\phi = 0.0$) if α_P is not larger than $\alpha_{PJ\max}\,\beta_{PJ}$ and increases rapidly to

$0.1^{C_{PJ}} - 1$ (i.e. $\phi = 0.1^{C_{PJ}} - 1$) when α_P exceeds $\alpha_{PJ\max}\,\beta_{PJ}$.

In the SIMMER-III code, ϕ is added (not multiplied) directly to the momentum exchange function K_{qs} between liquid phases and structures of the momentum Eq. (3-2). For pool flows where the effect of the structure is negligible, through this addition mathematic treatment, the effect of particle jamming can be considered by applying $K_{qs} = \phi$ to Eq. (3-2).

The particle jamming model was also mainly introduced for structure channel flows, and thus knowledge about its influence on pool multiphase flows with rich solid particles is limited. In this study, the effect of this model will also be discussed.

3.5 Simulation geometry for the experiments

Figure 6 shows a schematic view of the analytical geometry used in the SIMMER-III calculations for the corresponding experimental apparatus shown in Fig. 2. A two-dimensional cylindrical geometry is adopted. Taking the size of the solid particles into consideration, computational cell sizes adaptable to each part of the experimental setup were used. In the radial direction, 13 cells are defined while the axial direction has 128 cells. For the water pool, there are 83 cells in the axial direction.

4 Sensitivity analysis of models

Sensitivity analysis of the particle jamming and particle viscosity models has been performed based on experimental results of the cases with a 50 mm height particle bed formed from YB, BB and Al$_2$O$_3$ balls. The experimental results of those cases show very similar transient behaviors, although the absolute values in pressure transients and gas volume changes, as well as the surface height change of the particle bed, do show some differences. Therefore, comparisons between the experimental and simulated results of five selected cases will be presented in this Chapter for the sensitivity analysis of models.

The detail SIMMER-III input parameters of the five selected cases are listed in Table 2. The first case has an initial nitrogen gas pressure of 0.304 MPa and YB balls were used to form the particle bed with an initial particle volume fraction of 0.65. The second and third cases have an initial nitrogen gas pressure of 0.296 MPa and 0.199 MPa, respectively. The particle beds of these two cases were made of BB balls with an initial particle volume fraction of 0.61. In the fourth case, which has an initial nitrogen gas pressure of 0.301 MPa, Al$_2$O$_3$ balls were used to form the particle bed with an initial particle volume fraction of 0.64.

In the following sub-sections, the gas volume changes and the pressure transients of the above four cases will be presented. For particle bed movement, the results of two cases using BB balls forming the particle bed with an initial particle volume fraction of 0.61 will be presented. One of these cases is the above-mentioned second case with an initial nitrogen gas pressure of 0.296 MPa. The other case (the fifth case) has an initial nitrogen gas pressure of 0.237 MPa.

Simulated results both with and without the application of the viscous diffusion term coupled with the particle viscosity model will be presented together with their corresponding experimental results. In all of the following figures, VDT ON/OFF refers to simulations by the SIMMER-III code with (ON) and without (OFF) the viscous diffusion term coupled with the particle viscosity model.

This Chapter will only describe comparisons between experimental results and results simulated by different model combinations for the verification of the validity of models. The description and explanation of the experimental results (experimental dynamic behaviors) themselves will be presented in Chapter 5.

4.1 Gas volume change

Figures 7 to 10 show comparisons of the nitrogen gas volume change in the water pool together with that in the pressure vessel between experimental and simulated results of the selected four cases, respectively.

Experimental data for the total nitrogen gas volume changes in the water pool together with that in the pressure vessel were obtained from the water level changes in the upper pipe of the experimental setup, which were recorded by one of the high-speed cameras. Here, gas volume changes are defined as the difference of the total gas volume both in the water pool and the pressure vessel between at each moment and the beginning of the experimental period. Meanwhile the corresponding SIMMER-III simulated results were obtained directly from the total nitrogen gas volume changes in both the water pool and the pressure vessel. The time zero is hereafter defined by the triggering of the diaphragm rupture.

Comparisons between the simulated and experimental results of all four cases show that the SIMMER-III simulation with the particle viscosity model coupled with the viscous diffusion term gives poor results. It can also be seen from these figures that the results simulated by the SIMMER-III code without the viscous diffusion term agree quite well with their experimental counterparts in the first nitrogen expansion and the following compression process.

The simulation results shown in Figs. 8 and 9 indicate that the negative influence of the viscous diffusion term becomes much more obvious when the initial pressure of the nitrogen gas is much lower. This may be because the smaller driving force for the solid particles leads to the dominant effect of the particle viscosity model used in the viscous diffusion term. A comparison of simulation results among the cases performed under almost the same initial pressure shows the influence of the initial particle volume fraction on the viscous diffusion term. It can be seen from Fig. 8 that the viscous diffusion term with an initial particle volume fraction smaller than the value of α_{MP} (= 0.62) exerts a smaller influence on the result in comparison with the cases in which the initial particle volume fraction exceeds the value of α_{MP} used in the particle viscosity model (Figs. 7 and 10).

These results follow the characteristics of the function used for the particle viscosity model, in which the effective viscosity will increase to a very large value, as shown in Fig. 4, when the solid particle volume fraction is approaching the maximum volume fraction of solid particles defined in Eq. (3-5). From the comparison between the experimental and simulated results with the viscous diffusion term coupled with the particle viscosity model, we can say that the viscous diffusion term coupled with the particle viscosity model underestimates the gas volume change. This may be because the particle viscosity model overestimates the effective viscosity appearing in the viscous diffusion term. With the overestimated effective viscosity, the resistance to the expansion of the nitrogen gas is in turn overestimated such that simulations with the viscous diffusion term give the underestimated results of the gas volume change shown in Figs. 7 to 10.

4.2 Pressure transients

Simulated pressure transients were obtained from the pressure data of the computational cells where pressure sensors are located. Figures 11 to 14 show comparisons of the pressure transients in the pressure vessel between the simulated and experimental results of the selected four cases, respectively.

Similar to what is shown in Figs. 7 to 10, the comparisons between the simulated and experimental results of all four cases show that the SIMMER-III simulation with the particle viscosity model coupled with the viscous diffusion term does not yield good results. Figures 11 to 14 also show that the lower the initial nitrogen gas pressure and the larger the initial particle volume fraction become, the worse the viscous diffusion term coupled with the particle viscosity model influences on the results of the pressure transients. The poor results shown in the pressure transients might also be explained with the possible overestimated effective viscosity appearing in the viscous diffusion term by the particle viscosity model.

Comparing the experimental results with the simulated results using SIMMER-III without the viscous diffusion term, it can be concluded that under the present experimental conditions, SIMMER-III without

the viscous diffusion term can reasonably represent the observed pressure decrease in the pressure vessel caused by the expansion of the initially pressurized nitrogen gas as well as the following pressure increase caused by the subsequent compression of the nitrogen gas.

4.3 Surface height change of the particle bed

During the experiments, one of the high-speed cameras was used for recording the particle bed behavior. However, due to the invisibility of the inside of the particle bed caused by the opacity of the particle bed, the information recorded by the camera consists of only the surface change information of the particle bed. In this section, a comparison of the surface height change of the particle bed will be performed between the simulated and experimental results. Because of the difficulty of recognizing the respective images of particles and bubbles through the camera, the particle bed surface height changes before the passing of bubbles through the particle bed, and in particular the data obtained in the first nitrogen expansion period, will be the main focus of the comparison.

From the discussion in the above sections, it is clear that the particle viscosity model coupled with the viscous diffusion term has less positive influence on the simulated results. In addition, the more tightly the solid particles are packed initially, the more enhanced the negative effect of the viscous diffusion term becomes. Therefore, in this and also the following sub-sections, the results of two cases with a relative smaller initial particle volume fraction will be discussed.

Figures 15 and 16 show the experimental and simulated results of the two cases using BB balls to form the particle bed with an initial particle volume fraction of 0.61 but with a different initial nitrogen pressure of 0.296 MPa and 0.237 MPa, respectively. There are obvious differences in the shapes of the particle bed between the experimental images and the images obtained from the simulation using the SIMMER-III code with the viscous diffusion term coupled with the particle viscosity model as shown in Figs. 17 and 18. Therefore, in Figs. 15 and 16, the experimental results are compared only with the simulated results without the viscous diffusion term in the SIMMER-III code.

The experimental data are obtained by calculating the surface height change of the particle bed in the central-axial direction from the particle bed images recorded by the high-speed camera. The simulation results of SIMMER-III are defined in such a way that if the particle volume fraction, along with the central axis of the leftmost cells defined in Fig. 6, is no less than 0.10 in a computational cell, then the axial height of this computational cell will be counted in the particle bed height. As a result, the height change obtained from the SIMMER-III simulation indicates a step change, as shown in Figs. 15 and 16.

Taking the axial cell sizes and step change into consideration, it can be said that the results simulated by SIMMER-III without the viscous diffusion term agree well with their counterparts for the particle bed movement caused by the expansion of the nitrogen gas.

4.4 Images of the particle bed

Besides the quantitative comparison presented in the above sub-sections, a visual comparison will be presented here between the simulation and experimental results on the transient behavior of the particle

bed in the water pool. From the above discussion, it could be said that SIMMER-III without the viscous diffusion term can reasonably represent the transient behavior against the pressure transient of the initially pressurized nitrogen gas. Images of this transient process of the particle bed coming from one of the high-speed cameras are compared with the simulated images. Figures 17 and 18 show images of the particle bed of the same two cases described in the above section 4.3.

For a comparison between simulated images and their corresponding experimental counterparts, in Figs. 17 and 18, frames taken at the times of 20 ms, 60 ms, 100 ms, 150 ms, 200 ms, and 250 ms are shown. In these figures, both the images coming from the camera and the simulated results represent a region of 310 mm (diameter of the inner cylindrical water pool) × 325 mm (height). The base of the images corresponds to the axial location of the iron sieve (Fig. 2), which is 10 mm below the bottom of the water pool.

In Figs. 17 and 18, the first column, labeled "Exp.," lists the experimental images, while the other columns show the SIMMER-III simulation distribution images of the total volume fraction of solid particles and nitrogen gas. The experimental images show rough information regarding the movement of the solid particle and nitrogen-gas mixture inside the water pool. Although it is difficult to compare the detailed phase distributions because of the poor visibility of the particle bed under the current experimental conditions, the rough boundary images can be compared from these images.

It can be seen from Figs. 17 and 18 that the SIMMER-III simulations with the viscous diffusion term coupled with the particle viscosity model give quite different images from the experimental ones. As explained in Sections 4.1 and 4.2, this may be because the effective viscosity overestimated by the particle viscosity model causes larger resistance to the upward movement of the mixture. A comparison between Figs. 17 and 18 shows that the lower initial nitrogen gas pressure leads to a larger effect on the particle bed movement in the simulation. This is because less dispersal behavior of the solid-particle phase, which is caused by the lower initial pressure, results in the dominant influence of the particle viscosity model.

Comparing the experimental images with the images from the simulated results using SIMMER-III without the viscous diffusion term, Figs. 17 and 18 visually support the agreement between the simulated and experimental results of the surface height change of the particle bed, shown in Figs. 15 and 16, respectively. The images at 200 ms and 250 ms show the behavior of the nitrogen bubble, which is passing through the particle bed. Based on such a qualitative comparison, the general movement trend shown by the SIMMER-III simulation agrees well with the results of the experiments.

4.5　Discussions on the sensitivity analysis of models

In the experimental simulations using SIMMER-III, the effect of the particle jamming model and the particle viscosity model was examined. What needs to be explained is that the effect of the particle viscosity model is considered separately with respect to two aspects. One aspect is that applied in $K_{qq'}$ of the fluid-fluid drag term, and the other is considered by observing the effect of the viscous diffusion term coupled with the particle viscosity model.

Thus, comparisons were performed between the experimental results and their corresponding simulated results using the SIMMER-III code both with and without the viscous diffusion term coupled with the particle viscosity model. They show that the viscous diffusion term coupled with the particle viscosity model has no 'positive' but some 'negative' influences on the results. The reason for this may be because the particle viscosity model used overestimates the effective viscosity appearing in the viscous diffusion term. The comparisons also indicated that SIMMER-III without the application of the viscous diffusion term can well represent the dynamic behavior of the particle bed in a water pool caused by the pressure transient of the initially pressurized nitrogen gas in the pressure vessel under the present experimental conditions.

Moreover, further comparisons between the results indicate that the particle viscosity model applied in $K_{qq'}$ and the particle jamming model show no obvious influence on the simulated results of the pressure transients, the gas volume change in the water pool, the pressure vessel, or the surface height change of the particle bed, although the simulated results do indicate that the particle jamming model has some influence on the solid particle phase distribution inside the particle bed. In the SIMMER-III simulation for the current three-phase system of water, solid particles, and nitrogen gas, the particle viscosity model works in the momentum exchange functions $K_{qq'}$ between water and the nitrogen gas. This means that the particle viscosity model applied in $K_{qq'}$ only works in computational cells where all three phases (water, solid particles, and nitrogen gas) exist. On the other hand, under the present experimental conditions, there are few solid particles in most computational cells, in which nitrogen gas exists. The low concentration of solid particles in these computational cells leads to the decrease of the effect of the particle viscosity model.

The particle jamming model, which was originally introduced for channel flows especially effective in a one-dimension condition, did not show any obvious influence on the results. This may be due to the outward movement in the current experiments in the water pool with two-dimensional simulations since this outward movement could also dilute the concentration of the solid particles to be less than the maximum volume fraction defined in the jamming model and in turn decrease the effect of the particle jamming model.

4.6 Summary of the sensitivity analysis

Comparisons between the results of the SIMMER-III simulation and its corresponding experiments demonstrated that SIMMER-III without the application of the viscous diffusion term reasonably represents the dynamic behavior of pool multiphase flows with a 50 mm height solid particle bed formed from YB, BB and Al_2O_3 balls.

Model validations indicated that the viscous diffusion term coupled with the particle viscosity model show some obvious 'negative' effects on the results. Such results are caused by the coupled particle viscosity model, which overestimates the effective viscosity in the viscous diffusion term. This may be also because the present experiments were performed under a quite lower pressure range and because the initial solid particle volume fractions are very close or even exceed the maximum volume fraction of solid

particles defined in the particle viscosity model. Moreover, the applicability of the particle viscosity model, which has been verified in experiments with rather small particles, to mixtures with a wider range of volume fraction and much larger particles needs to be investigated.

In addition, the particle viscosity model applied in the momentum exchange function and the particle jamming model showed no obvious influence on the obtained transient characteristics. Thus it is thought that the outward movement of the particles after the injection of the gas phase dilutes the concentration of the solid particles in computational cells, which in turn decreases the effect of the two models. Simulated results did show, however, some influences of the particle jamming model on the solid particle phase distribution, for which currently no experimental data is available. Further experiments therefore are necessary for verification of the particle jamming model.

5 Analysis of the multiphase flow experiments

Based on the results of sensitivity analysis of models in Chapter 4, the SIMMER-III simulations were done for all of the experimental cases performed, without the application of the viscous diffusion term, to verify whether the SIMMER-III code can well represent the characteristics of the pool multiphase flows with various particle beds formed from different types of particles.

5.1 Comparisons between different experimental cases

In the experiments, the initial pressure of the nitrogen gas in the pressure vessel and the type of particles forming the particle beds with different bed heights were taken as experimental parameters. Experimental results for all cases show very similar transient histories, while the absolute values of the gas volume change, and also the pressure transients, exhibit some differences. In the following parts, the differences caused by different particle beds will be compared, and the simulated results afforded by the SIMMER-III code will be presented and discussed together with their corresponding experimental results.

5.1.1 Gas volume changes

The same as in Chapter 4, gas volume changes defined here correspond to the differences between the instantaneous nitrogen gas volumes in the experimental processes and the initial nitrogen gas volumes at the beginning of the experiments. Experimental data for the total gas volume changes in both the water pool and the pressure vessel were obtained from the water level changes in the upper pipe of the experimental setup. While the corresponding SIMMER-III simulated results were obtained directly from the total nitrogen gas volume changes in both the water pool and the pressure vessel. The time zero is hereafter defined by the triggering of the diaphragm rupture.

(1) Different initial nitrogen gas pressures

The difference shown in the gas volume changes caused by various initial nitrogen gas pressures in the experimental cases, using the same particle bed height, is particularly obvious for each particle type used. Here, the experimental results of cases obtained using a 50 mm height YB ball bed will be explained as an example.

Figure 19 shows the experimental and corresponding simulated results of the gas volume changes for the three cases in which different initial nitrogen gas pressures were used. Both the experimental and simulated results for all three cases show that once the rupture disk has broken, the nitrogen gas volume begins to increase with the expansion of the originally pressurized nitrogen gas in the pressure vessel, while tens of seconds later the nitrogen gas volume starts to decrease. This occurs because, as the nitrogen gas expands, the pool water as well as the particle bed is accelerated upward till the nitrogen-gas pressure decreases to its surrounding pressure. At this moment, since the pool water and the particle bed have their maximum upward velocity, they are still driven upward by an inertial force of the water slug but with a decelerated motion. As a result, the nitrogen gas continues to expand out of the pressure vessel and its pressure can decrease to a value lower than the atmospheric pressure, as can be seen from Figs. 8 and 9 etc. Later, the decelerated pool water and the particle bed reverse their motion backward compressing the

expanded nitrogen gas. This leads to the decrease of the nitrogen gas volume.

By comparing the experimental results for the three cases shown in Fig. 19, it can be seen that when the initial nitrogen gas pressure is higher, the corresponding gas volume change (especially the maximum gas volume change) is much greater than that in the cases where a lower initial nitrogen gas pressure is used. The experimental results also show that the higher the initial pressure, the longer the expansion period of the nitrogen gas. On the other hand, Fig. 19 shows that these differences between the experimental cases are well presented by the corresponding simulations.

(2) Different kinds of particles (different densities)

Figure 20 shows comparisons of the maximum gas volume changes between experimental cases in which a 50 mm height bed is formed from solid particles of different densities. It should be mentioned here that efforts to fabricate the polyester resin rupture disks so that they break at the same initial nitrogen gas pressure has proven difficult. Therefore, only the results of experimental cases having the same initial nitrogen gas pressures are to be compared in this and the next subsections.

As can be seen from Fig. 20, when the initial nitrogen gas pressure is the same, the heavier particles cause a smaller maximum gas volume change. This occurs because for particle of higher density, the drag force in the nitrogen gas upward expansion process becomes greater. As a result, the momentum loss experienced by the nitrogen gas is larger and, in turn, the maximum gas volume change is smaller. Figure 20 also shows that the difference between the maximum gas volume changes in the experimental cases with a higher initial nitrogen gas pressure is more obvious than that between cases with a lower initial nitrogen gas pressure. This may indicate that the differences caused by the various initial nitrogen gas pressures are more remarkable than that caused by different particle densities, which may be because the particles with a smaller density are already very heavy when driven by the currently used pressures so that a relatively large difference cannot be obtained when heavier particles are used.

The simulated maximum gas volume changes are shown with respect to their experimental results in Fig. 20. Comparing the simulated and experimental data points given by circles and squares, respectively, it is clear that the simulated results are very close to their experimental counterparts.

(3) Different particle bed heights

Figure 21 shows comparisons of the maximum gas volume changes between experimental cases with different particle bed heights. Comparing the experimental cases when SS ball beds with a 50 mm and 100 mm height are used, it can be seen that when the initial nitrogen gas pressure is the same, the higher particle bed heights result in smaller maximum gas volume changes. This is because higher particle bed heights cause a larger resistance to the expansion of the nitrogen gas, which as a result causes a smaller maximum gas volume change. Comparing the cases with SS balls, Fig. 21 shows that the higher the initial nitrogen gas pressure, the greater the difference in the maximum gas volume changes is between cases with different particle bed heights. This may also be because SS particle beds with a lower height are already heavy enough when compared to the initial driving pressure. The comparison between cases in which 200

mm and 300 mm height Al_2O_3 beds are investigated shows that there is some difference between the maximum gas volume changes. However, the difference is not as large as that shown between the cases in which 50 mm and 100 mm height SS ball beds are used. This may be because the initial nitrogen gas pressure is high enough to move lighter Al_2O_3 particles upward in the two cases even with relatively high particle beds.

The simulated results presented in Fig. 21 agree well with their corresponding experimental results. Agreements shown in Figs. 19 to 21 indicate that the SIMMER-III code can well represent the dynamic behavior induced by pressure transients of the various particle beds, in a liquid pool.

5.1.2 Pressure transients

Changes in the types of particles or the particle bed heights used show certain difference in the corresponding pressure transients, both in the pressure vessel and at the top of the water pool. However, the pressure transient data obtained at the top of the water pool has some short-period oscillations, which could be related to the natural frequency of the acrylic cylindrical structure.[21] Therefore, it becomes difficult to compare the differences between the absolute values caused by different particle beds. Nevertheless, SIMMER-III is in good agreement with the general trend of these pressure histories. Here, the results of one case will be given as an example. Figure 22 shows a good agreement between the experimental and SIMMER-III results of the pressure transient at the top of the water pool of an experimental case that has an initial nitrogen gas pressure of 0.246 MPa and an Al_2O_3 bed height of 100 mm.

Meanwhile, the differences between the experimental and SIMMER-III results shown at the pressure transients in the pressure vessel are not very large, although they did cause the differences in the gas volume changes, as discussed in the above section. As shown in Fig. 23, there are no remarkable differences between the pressure transient observed in the experimental case, in which a 300 mm height Al_2O_3 bed is used, and that obtained in the case without a particle bed. This may be because the initial water height, which was at the level of 115 mm in the upper pipe, is so high that its influence on the pressure transients in the pressure vessel is of a greater significance.

Therefore, experimental cases in which a lower water height (typically 300 mm lower than the height of the top of the cylindrical water pool) was used in the water pool, were performed in order to observe whether obvious differences in the pressure transients were apparent between experimental cases with and without a particle bed, and also to verify if SIMMER-III can well represent this possible difference.

Figure 24 shows a comparison of the pressure transients in the pressure vessel in the case of a lower water height between the experiments performed with and without a 300 mm height Al_2O_3 bed in the water pool. Comparing the experimental data shown in Fig. 24, when no particle bed is present in the water pool, the nitrogen gas expands and its pressure decreases to the lowest value in the first nitrogen expansion period faster than it does in the experimental case in which a 300 mm height particle bed is present. This is because the pressure resistance experienced by the nitrogen gas in the water pool without any particle bed is smaller than that when a 300 mm height Al_2O_3 bed is present. This difference in the first nitrogen expansion period, together with the existence of the solid particle bed, causes the subsequent difference

shown in the pressure transients.

Results obtained from the computational simulations shown in Fig. 24 agree well with the corresponding experimental results. The difference shown in the pressure transients between the two experimental cases are also well described.

Difference between Figs. 23 and 24 indicates that the water height has influence on the experimental behavior or it can be concluded that the flow behavior of experiments described in Chapter 2 are liquid dominant. In order to obtain experimental results that show a much greater influence of the solid particle beds, especially the influence of the particle-particle interactions on the transient behaviors, it may be better to use a much lower water height compared to the particle bed height.

5.2   Simulations of experiments with a 50 mm bed

As having been said, the general behavior of all cases performed under the experimental conditions descried in Chapter 2 is similar. Therefore, results of one case using SS balls will be reported as a representation of the results obtained for all cases with a 50 mm particle bed in the water pool. In this case, a 50 mm height SS ball bed is driven by the expansion of nitrogen gas with an initial pressure of 0.318 MPa.

5.2.1   Pressure transients

Figure 25 shows the pressure transients in the pressure vessel and at the top of the water pool for the experimental case where the 50 mm height bed is employed, respectively. In Fig. 25, "P1" defines the pressure in the pressure vessel and "P2" represents the pressure at the top of the water pool. Pressures were obtained at the two measuring points via the two pressure sensors (PT), as sketched in Fig. 2. Simulated pressure transients were obtained from the pressure data of computational cells, where the two pressure sensors are located.

The experimental results indicated by "P1" in Fig. 25 show that in the pressure vessel, the nitrogen gas pressures decrease rapidly after the rupture disk breaks due to the expansion of the originally pressurized nitrogen gas. When the pressure decreases to its minimum value, which is much lower than atmospheric pressure, it starts to increase because of the subsequent compression of the nitrogen gas by the surrounding materials. Then, when the pressure becomes greater than its surrounding pressure, the nitrogen gas expands causing the pressure to decrease again, as shown in Fig. 25. Over a much longer time scale, it is foreseeable that the pressure transient in the pressure vessel will continue this decrease-increase process until the pressure finally arrives at a steady-state value. Simulated results given by the solid lines in Fig. 25 show that the pressure transients in the pressure vessel obtained by SIMMER-III agree well with their corresponding experimental results.

Moreover, Fig. 25 shows that the pressure at the top of the water pool rapidly increases to its first peak value in about 10 ms, mainly caused by the sudden ejection of the nitrogen gas from the pressure vessel. This pressure then varies as a result of the response to the pressure transient in the pressure vessel, i.e. when the pressure is at its minimum value, the pressure at the top of the water pool is also at a

minimum; but when the pressure in the vessel increases to another peak value, the pressure at the top of the water pool also arrives at a peak value. A general trend of the pressure history calculated using SIMMER-III shows good agreement with the experimental measurements. Moreover, these simulated results also well represent the concomitance that the pressure transient at the top of the water pool changes as an immediate response to the transient of the pressure in the pressure vessel.

5.2.2 Gas volume change

Figure 26 shows gas volume changes obtained in the experiment and the SIMMER-III simulation for the case in which 50 mm height bed is employed. In this figure, images of the 50 mm particle bed at t = 75 ms and t = 158 ms are also compared between the experiment and the SIMMER-III results in connection with the gas volume changes at the same instances. The two experimental images (labeled "Exp.") obtained using a high-speed camera, together with the corresponding SIMMER-III simulated images, represent the same region as defined in Chapter 4 for Figs. 17 and 18. The SIMMER-III simulated results show images described by isolines representing the distribution of the total volume fraction of SS balls and nitrogen gas (labeled "SS Ball + N_2 (SIMMER-III)"), and the phase distribution of the nitrogen gas only (labeled "N_2 (SIMMER-III)").

As seen in Fig. 19, Fig. 26 also shows that the gas volume firstly increases due to the expansion of the nitrogen gas, and then decreases because of the subsequent compression of the nitrogen gas, causing the nitrogen gas pressure to increase and, in turn, expand, resulting in an increase in the volume again.

By comparing the experimental and simulated results for the gas volume changes, it can be seen that SIMMER-III shows good agreement with the experimental results. In Fig. 26, the experimental results show that the gas volume change arrives at its maximum value at 75 ms and the subsequent minimum value at about 158 ms. The simulated phase distribution isoline of the nitrogen gas at these two instances also show that the nitrogen bubbles are at their largest and subsequent smallest, respectively, thus providing visual evidence to support the agreement in the gas volume changes between the simulated and experimental results.

5.2.3 Particle bed images

Figure 27 shows image comparisons between the experimental and simulated results, in which the region shown corresponds to the same region as defined for images shown in Fig. 26. Moreover, as described in the above sub-section, the two images types (labeled "SS ball + N_2 (SIMMER-III)" and "N_2 (SIMMER-III)") expressed by isolines obtained from the SIMMER-III simulated results in Fig. 27, also represent the total volume fraction distribution of SS balls and nitrogen gas, and the phase distribution of the nitrogen gas only, respectively. Frames taken at 20, 60, 100, 160 and 200 ms are shown for comparison.

The experimental images obtained show that in the early period after the experiment begins, the particle bed continues to move upward due to the quick ejection of the initially pressurized nitrogen gas from the pressure vessel. Then at 100 and 160 ms, the experimental images show some of the particles splashing down from the top surface of the particle bed. This occurs because the nitrogen gas volume

becomes steadily smaller in this period, and the velocity of the particles shows a corresponding decrease such that some of the particles are observed flowing back towards the body of the particle bed. The frame at 200 ms shows that part of the nitrogen gas has already passed through the particle bed and that a large number of solid particles are in the process of falling back towards the body of the particle bed.

The column (labeled "N_2 (SIMMER-III)") in Fig. 27 shows the SIMMER-III simulated isoline images of the movement of the nitrogen gas in the water pool. From 20 to 200 ms, the images show that the nitrogen gas volume increases, decreases, and then increases again. Finally, the nitrogen gas passes through the particle bed and moves upward through the water pool. The simulated movement images of the nitrogen gas can be used to explain the experimental movement process of the particle bed described in the above paragraph; i.e. the particle-bed upward moving period, a particle splashing down and falling back period, and also the nitrogen gas passing through the particle bed period. The particle bed moving processes as well as the pressure transients shown in Fig. 25 occur as a response to the movement of the nitrogen gas as shown by the simulated images.

The simulated movement of the particle bed shown by the volume fraction isolines in the second column (labeled "SS Ball + N_2 (SIMMER-III)") of Fig. 27 has similar boundary shapes as that shown by the experimental images. The above discussions and comparisons of the experimental and simulated images indicate that the SIMMER-III code well represents the movement of the 50 mm height particle bed in the water pool.

5.3   Simulations of experiments with a 100 mm bed

Experiments with a 100 mm height particle bed were performed with SS and Al_2O_3 balls, respectively. All parameters of results examined for those experimental cases are the same as described in the above sections, therefore, results in this part will be simply explained through figures. Two typical cases will be shown here. The first case employs a 100 mm height SS bed driven by the expansion of nitrogen gas with an initial pressure of 0.313 MPa, while the second uses an Al_2O_3 bed of 100 mm height, in which the initial nitrogen gas pressure is 0.308 MPa.

The pressure transients of the two cases are shown in Figs. 28 and 29, while Figs. 30 and 31 show the gas volume changes of the two experimental cases, respectively. As can be seen from these figures, good agreements between the experimental and simulated results are obtained again for the cases with a 100 mm height particle bed. Under the current initial nitrogen gas pressure range, there is not much movement of the 100 mm height SS ball bed. Therefore, only particle bed images of the 100 mm Al_2O_3 bed are presented here. Image comparisons shown in Fig. 32 visually proofs the agreement between experimental and SIMMER-III simulated results.

5.4   Simulations of experiments with a 200 and 300 mm bed

Under the currently available initial pressure conditions, there is no much obvious transient in the particle bed surface of experiments with a 200 and 300 mm Al_2O_3 bed. Actually those cases were performed mainly for the purpose of checking the pressure transients in the pressure vessel. Since with

such kinds of high particle beds, the resistance to the nitrogen gas expansion as well as the friction between phases is considered to be much more larger than cases with a 50 or 100 mm Al_2O_3 bed, which will in turn influence the pressure transients. In addition, results, i.e. the gas volume change, obtained from the water level change in the upper pipe shown in Fig. 2 can also be verified.

For each kind of particle bed height, results of one typical experimental case will be presented. For the case employing a 200 mm height Al_2O_3 bed, the initial pressure is 0.248 MPa, while the other case with an Al_2O_3 bed of 300 mm height, the initial nitrogen gas pressure is 0.251 MPa.

The pressure transients of the two cases are shown in Figs. 33 and 34, while Figs. 35 and 36 show the gas volume changes of the two experimental cases, respectively. Despite the high Al_2O_3 bed, the pressure transients and the gas volume changes simulated by SIMMER-III still well represent their experimental counterparts. These may indicate that the transient behaviors are still mainly controlled by the liquid phase in the pool.

5.5 Summary and discussion

In this chapter, analyses of the experiments described in Chapter 2 were performed. A comparison of all of the experimental cases, despite the differences between the particle beds, showed that all cases have very similar transient trends in their dynamic behaviors, which further indicate that the current experiment behaviors are liquid dominant.

The simulated results obtained using the SIMMER-III code showed good agreement with respect to their experimental counterparts, and the differences in the experimental results are also well represented by SIMMER-III. The analysis in this Chapter indicated that the SIMMER-III multiphase fluid-dynamics models is applicable for representing the behavior of multiphase flow with solid phase when the liquid phase is dominant in the dynamic behavior.

6 Concluding remarks

In this study, a series of experiments was performed to verify the validity of SIMMER-III in simulating the pool multiphase flows with rich solid particles. Sensitivity analysis of models showed that the viscous diffusion term coupled with the particle viscosity model did not contribute to improve the simulations and further experiments for the verification of the particle jamming model are necessary.

Although the viscous diffusion term has been introduced to SIMMER-III for the investigation of the effect of bubbles on the behavior of a molten pool, SIMMER-III without this term reasonably represented the behaviors of the performed experiments. The results of simulation indicated that although there is no consideration of an additional pressure field for the solid phase in the momentum equation of the solid phase, SIMMER-III can still be applied for representing the behavior of multiphase flows with solid phase when the liquid phase is dominant in the dynamic behavior.

For future work, SIMMER-III code verification of its validity on representing particle dominant multiphase flow behaviors will be of significance.

References

1) Kondo, Sa., Tobita, Y., Morita, K., et al., 1992. SIMMER-III: an advanced computer program for LMFBR severe accident analysis. In: Proc. Int. Conf. on Design and Safety of Advanced Nuclear Power Plant (ANP '92), Tokyo, Japan, 25-29 October, pp. 40.5.1-40.5.11.

2) Tobita, Y., Kondo, Sa., Yamano, H., et al., 2000. Current status and application of SIMMER-III, an advanced computer program for LMFR safety analysis. In: Proc. 2nd Japan-Korea Symposium on nuclear Thermal Hydraulics and Safety (NTHAS2), Fukuoka, Japan, 15-18 October, pp. 65-72.

3) Bohl, W.R., Wilhelm, D., Parker, F.R., et al., 1990. AFDM: An advanced fluid-dynamics model. Los Alamos National Laboratory, LA-11692-MS.

4) Bohl, W.R. and Luck, L.B., 1990. SIMMER-II: a computer program for LMFBR disrupted core analysis. Los Alamos National Laboratory, LA-11415-MS.

5) Yamano, H., Fujita, S., Tobita, Y., et al., 2003. SIMMER-III: a computer program for LMFR core disruptive accident analysis -Version 3.A model summary and program description. Japan Nuclear Cycle Development Institute, JNC TN9400 2003-071.

6) Kamiyama, K., 2000. Analysis of THEFIS with particles. In: Phase 2 code assessment of SIMMER-III, a computer program for LMFR core disruptive accident analysis. Japan Nuclear Cycle Development Institute, JNC TN9400 2000-105, pp. A-283-A-303.

7) Tobita, Y., Momentum Exchange Function Model in SIMMER-III (Research Document), Japan Nuclear Cycle Development Institute, to be published.

8) Russel, W.B., 1983. Effects of interactions between particles and rheology of dispersions, in R.E.Meyer (ed.), Theory of Dispersed Multiphase Flow, Academic Press, New York, pp. 1-34.

9) Horie, H., Shirakawa, N., Tobita, Y., et al., 2001. The effect of bubble size on the radial distribution of void fraction in two-phase flow in a circular tube. Journal of Nuclear Science and Technology 38, 711-720.

10) Gidaspow, D., 1994. Multiphase Flow and Fluidization: Continuum and Kinetic Theory Descriptions. Academic Press, New York.

11) Ding, J. and Gidaspow, D., 1990. A bubbling fluidization model using kinetic theory of granular flow. AIChE Journal 36, 523-538.

12) Tsuji, Y., Kawaguchi, T., Tanaka, T., 1993. Discrete particle simulation of two-dimensional fluidized bed. Power Technology 77, 79-87.

13) Gera, D., Gautam, M., Tsuji, Y., et al., 1998. Computer simulation of bubbles in large-particle fluidized beds. Power Technology 98, 38-47.

14) Boemer, A., Qi, H. and Renz, U., 1997. Eulerian simulation of bubble formation at a jet in a two-dimensional fluidized bed. Int. J. Multiphase Flow 23, 927-944.

15) Taghipour, F., Ellis, N., and Wong, C., 2005. Experimental and computational study of gas-solid fluidized bed hydrodynamics. Chemical Engineering Science 60, 6875-6867.

16) Lun, C.K.K., Savage, S.B., Jeffery, D.J., et al., 1984. Kinetic theories for granular flow: inelastic particles in Couette flow and slightly inelastic particles in a general flow field. J. Fluid Mech. 140, 223-256.

17) Ishii, M. and Zuber, N., 1979. Drag coefficient and relative velocity in bubbly, droplet or particulate flows. AIChE Journal 25, 843-855.

18) Tobita, Y., Morita, K., Kondo, Sa., et al., 1991. Interfacial area modeling for a multiphase, multi-component fluid-dynamics code. In: Proc. Int. Conf. on Multiphase Flows, Tsukuba, Japan, 24-27 September, pp. 361-364.

19) Saunders, F.L., 1961. Rheological properties of monodisperse latex systems I. Concentration dependence of relative viscosity. Journal of Colloid Science, 16, 13.

20) Krieger, I.M., 1972. Rheology of monodisperse lattices. Advances in Colloid and Interface Science, 3, 111.

21) Morita, K., Tanoue, S., Matsumoto, T., et al., 2004. Improvement of a reactor safety analysis code SIMMER-III for transient bubble behaviors. In: Proc. 6th Int. Conf. on Nuclear Thermal Hydraulics, Operation and Safety (NUTHOS-6), Nara, Japan, 4-8 October, NP051.

Nomenclature

t	time (s)
v	velocity (m s^{-1})
P	pressure (Pa)
g	gravitational acceleration (m s^{-2})
$K_{qq'}$	momentum exchange function between components q and q'
K_{qs}	momentum exchange function between components q and structure
VM_q	virtual mass term
S	strain rate
$A_{qq'}$	viscous term defined for $K_{qq'}$
$B_{qq'}$	turbulent term defined for $K_{qq'}$
C_{PJ}	parameter defined in the particle jamming model

Greek letters

$\bar{\rho}$	macroscopic density (kg m^{-3})
υ	specific volume (m^3 kg^{-1})
α	volume fraction
α_{MP}	maximum volume fraction of solid particles defined in the particle viscosity model
$\alpha_{PJ\max}$	maximum packing volume fraction of solid phases defined in the particle jamming model
β_{PJ}	fraction of $\alpha_{PJ\max}$ above which the particle jamming model is applied
μ	viscosity (Pa s)
μ_C	effective viscosity of the continuous liquid phase
μ_L	viscosity of the continuous liquid phase
ϕ	particle jamming model function

Subscripts

q, q'	component of the three fluid phases
L	liquid phase
P	solid particles

Table 1: Initial experimental parameters.

Different kinds of particles were used for different particle bed heights. For a 50 mm height bed, YB (plastic particles), BB (plastic particles), Al_2O_3 and SS (stainless steel particles) balls were used to form the bed, respectively. For a 100 mm height bed, experiments were only performed with Al_2O_3 and SS balls, respectively. For 200 and 300 mm height beds, experimental cases using Al_2O_3 balls were performed.

Parameters	Values or ranges
Particle types (density (kg/m^3))	YB balls (1010); BB balls (2210); Al_2O_3 balls (3580); SS balls (7970)
Particle diameter (mm)	6
Particle bed height	50 mm (YB balls, BB balls, Al_2O_3 balls, SS balls) 100 mm (Al_2O_3 balls, SS balls) 200 mm (Al_2O_3 balls) 300 mm (Al_2O_3 balls)
Range of the initial nitrogen gas pressure	From around 0.2 to around 0.3 MPa

Table 2: Five experimental cases for model sensitivity analysis.

	1st Case	2nd Case	3rd Case	4th Case	5th Case
Particle type	YB balls	BB balls	BB balls	Al_2O_3 balls	BB balls
Particle density (kg/m^3)	1010	2210	2210	3580	2210
Particle diameter (mm)	6	6	6	6	6
Bed height (mm)	50	50	50	50	50
Initial nitrogen gas pressure (MPa)	0.304	0.296	0.199	0.301	0.237
Initial particle volume fraction	0.65	0.61	0.61	0.64	0.61
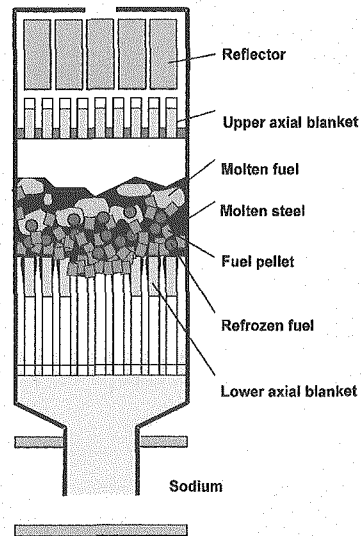
Fig. 1: Schematic view of a disrupted core with subassembly scale.
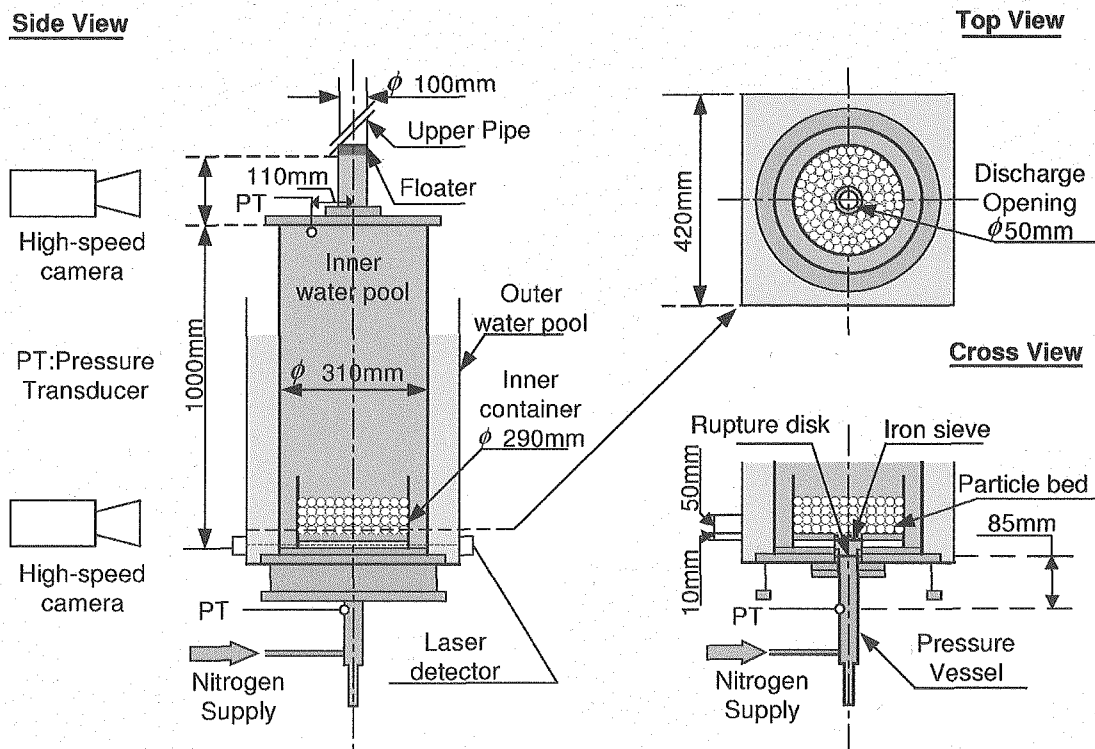
Fig. 2: Schematic view of the experimental apparatus.

The points for measuring pressure are indicated by PT. For experimental cases where 50 and 100 mm height beds were employed, the dimensions of the inner container are as shown in this figure. For experimental cases where 200 and 300 mm height particle beds were used, a taller inner container, with an inner diameter of 280 mm and a height of 510 mm, was used.
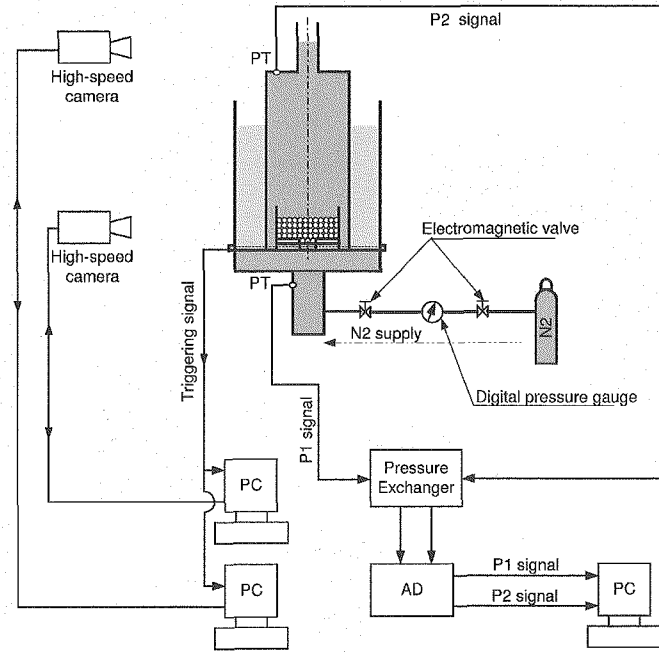
Fig. 3: Schematic view of the whole experimental system.

The nitrogen gas supply was controlled by two electromagnetic valves. The two high-speed cameras began to work after they received the triggering signal. Pressure signals obtained by pressure sensors were converted to DC voltage signal by the pressure and AD exchangers.
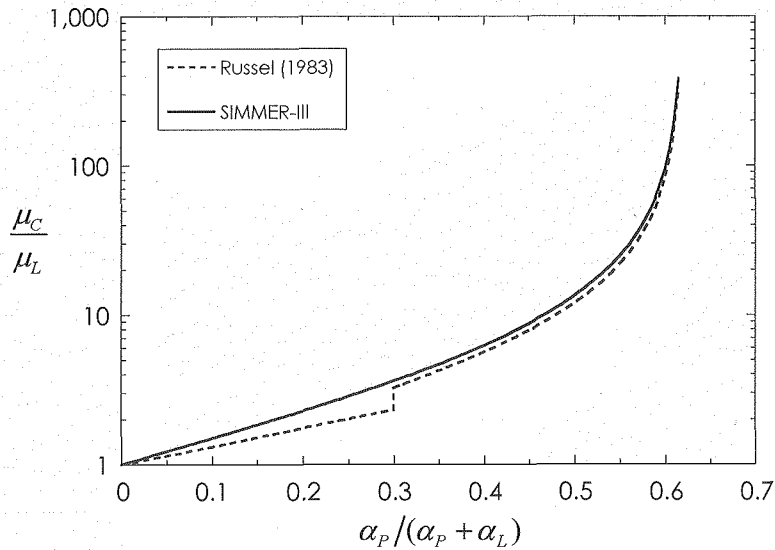
Fig. 4: Increase of effective viscosity due to existence of solid particles.

μ_C is the effective viscosity of the continuous liquid phase while μ_L is the viscosity of the continuous liquid phase. α_P and α_L is the volume fraction of solid-particle and liquid phases, respectively.
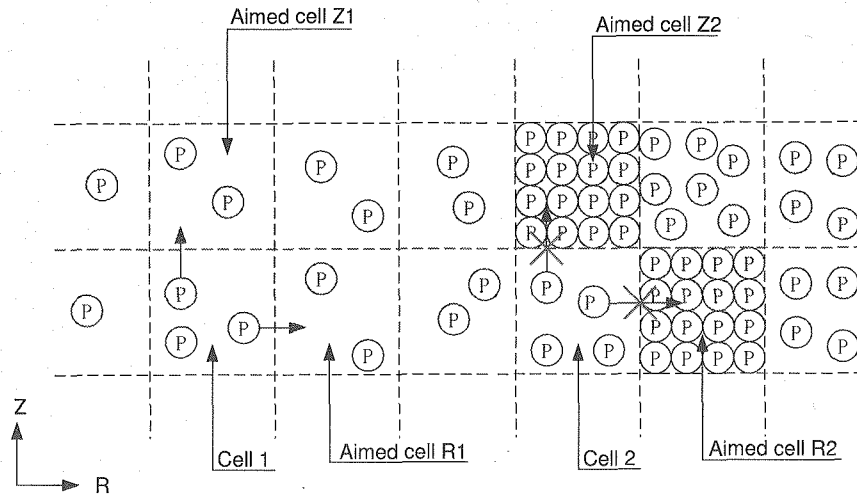
Fig. 5: Schematic view of particle jamming phenomenon.

"P" means particle. Particles in cell 1 can enter into the aimed cells R1 and Z1 because the particle volume fraction in cells R1 and Z1 is less than its maximum while particles in cell 2 cannot enter into the aimed cells R2 and Z2 because the particle volume fraction in cells R2 and Z2 is in its maximum.
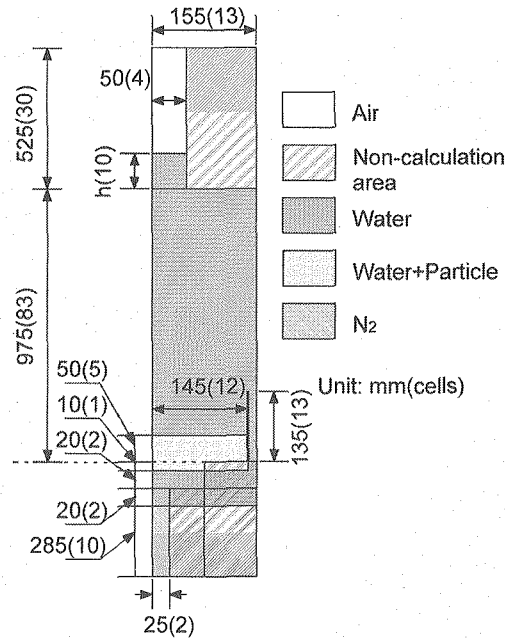
Fig. 6: Analytical geometry used for SIMMER-III simulation.

The analytical geometry is based on the experimental setup using the inner container shown in Fig. 2. For experimental cases where 200 and 300 mm height beds were used, a taller inner container, with an inner diameter of 280 mm and a height of 510 mm, was used. There is some adjustment of the analytical according to the size of the inner containers.
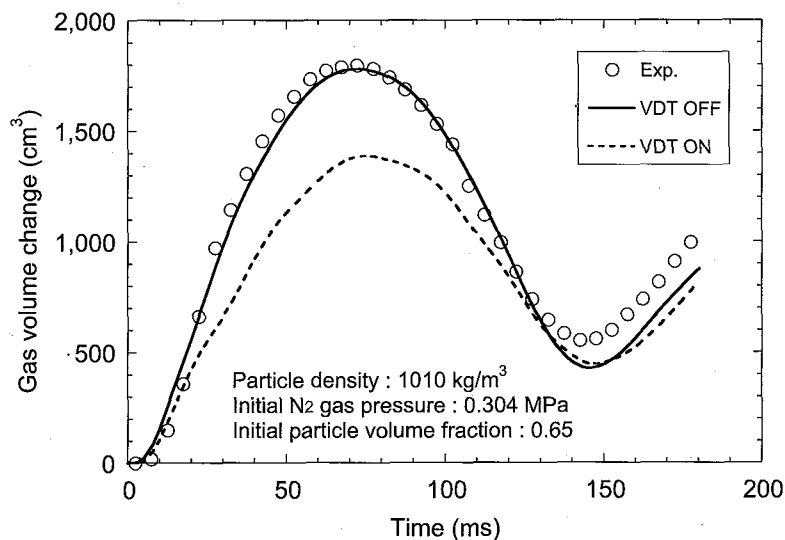
Fig. 7: Gas volume change in the water pool and pressure vessel for the 1st experimental case.

In this and all other figures, VDT ON/OFF refers to simulations by SIMMER-III with (ON) and without (OFF) the viscous diffusion term coupled with the particle viscosity model.
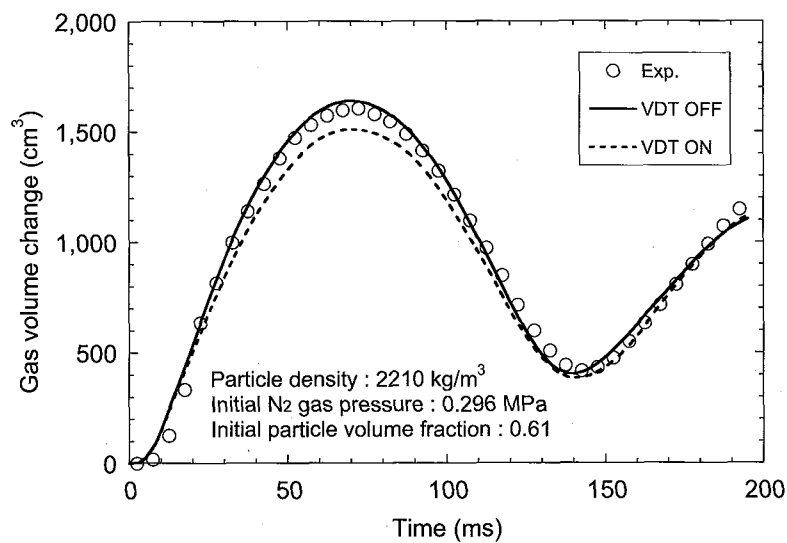
Fig. 8: Gas volume change in the water pool and pressure vessel for the 2nd experimental case.
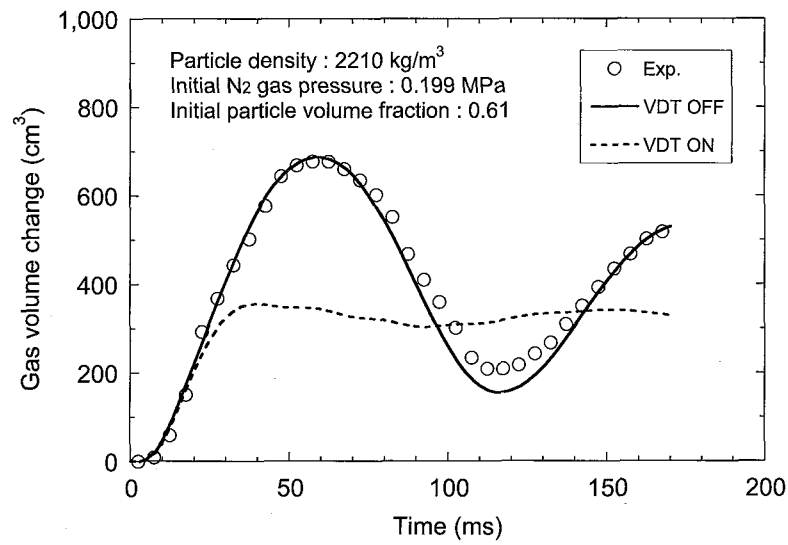
Fig. 9: Gas volume change in the water pool and pressure vessel for the 3rd experimental case.
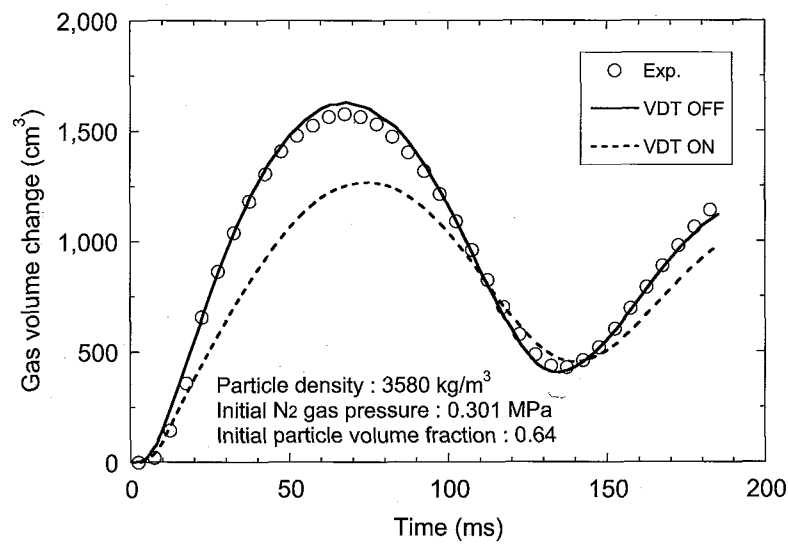
Fig. 10: Gas volume change in the water pool and pressure vessel for the 4th experimental case.
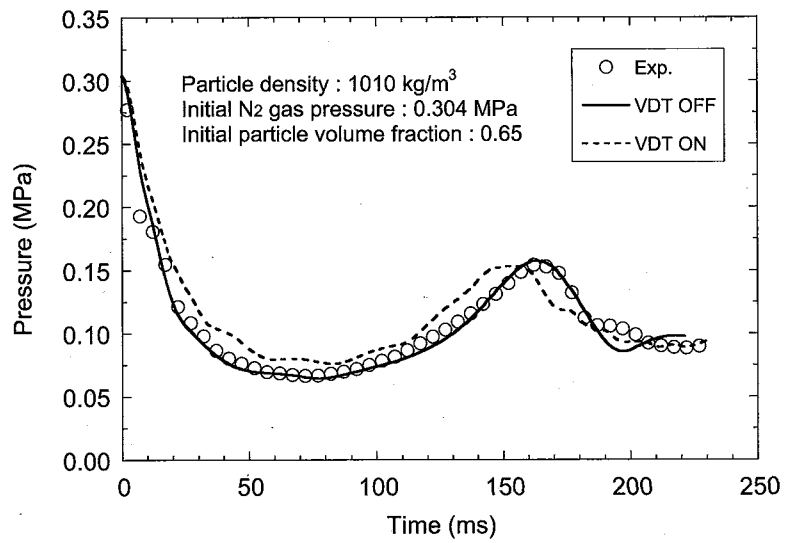
Fig. 11: Pressure transient in the pressure vessel for the 1st experimental case.
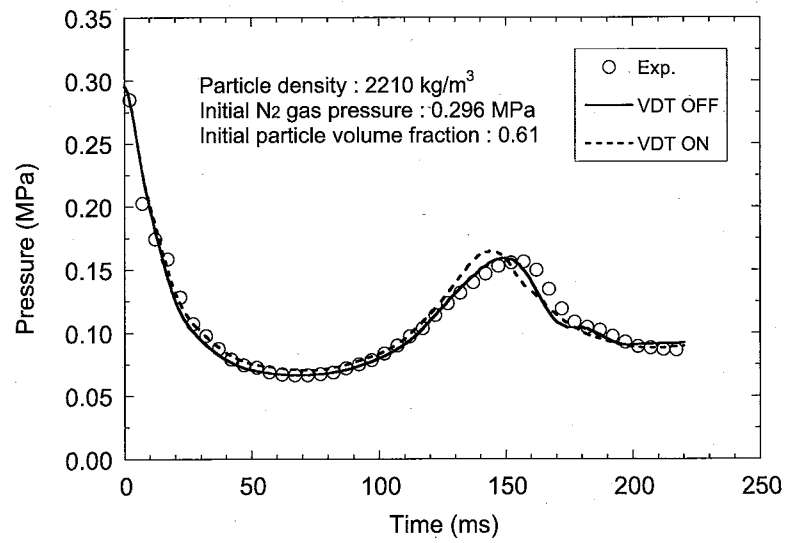
Fig. 12: Pressure transient in the pressure vessel for the 2nd experimental case.
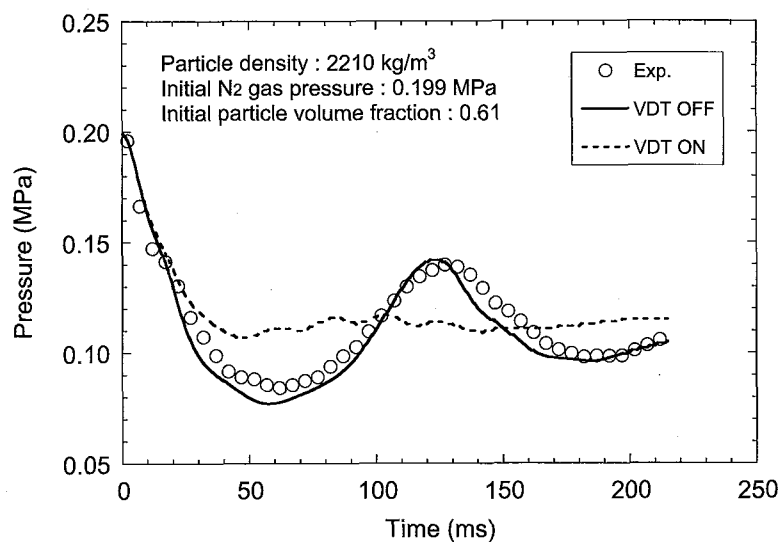
Fig. 13: Pressure transient in the pressure vessel for the 3rd experimental case.
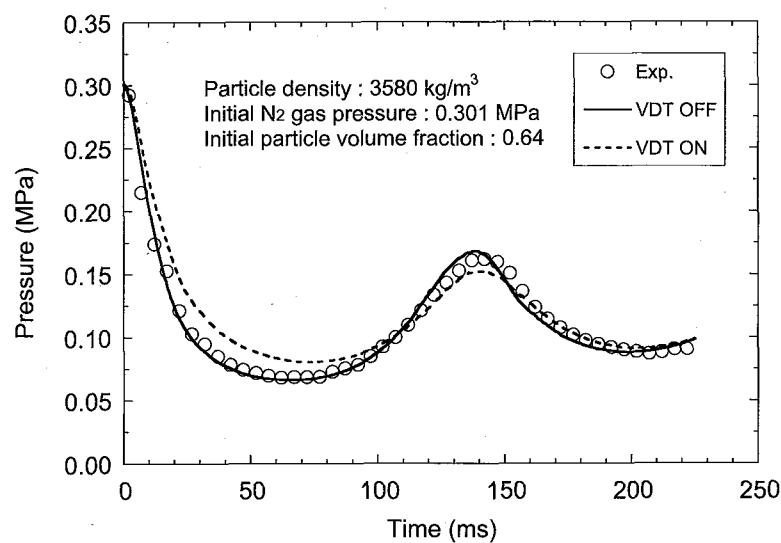
Fig. 14: Pressure transient in the pressure vessel for the 4th experimental case.
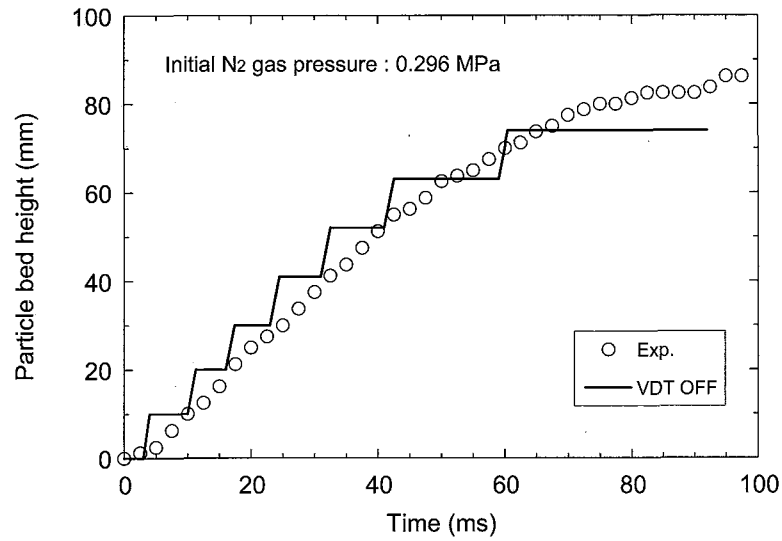
Fig. 15: Surface height change of the particle bed for the 2nd experimental case.

BB balls were used for the particle bed with an initial particle volume fraction of 0.61 and the initial nitrogen gas pressure was 0.296 MPa.
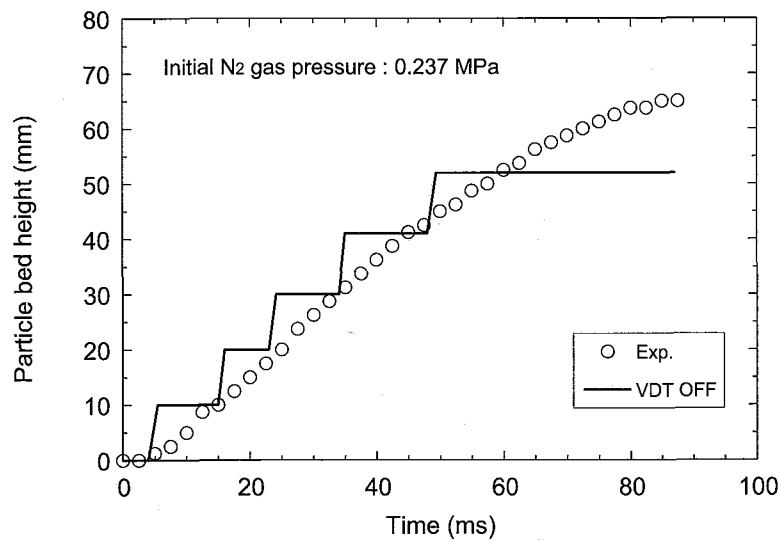
Fig. 16: Surface height change of the particle bed for the 5th experimental case.

BB balls were used for the particle bed with an initial particle volume fraction of 0.61 and the initial nitrogen gas pressure was 0.237 MPa.
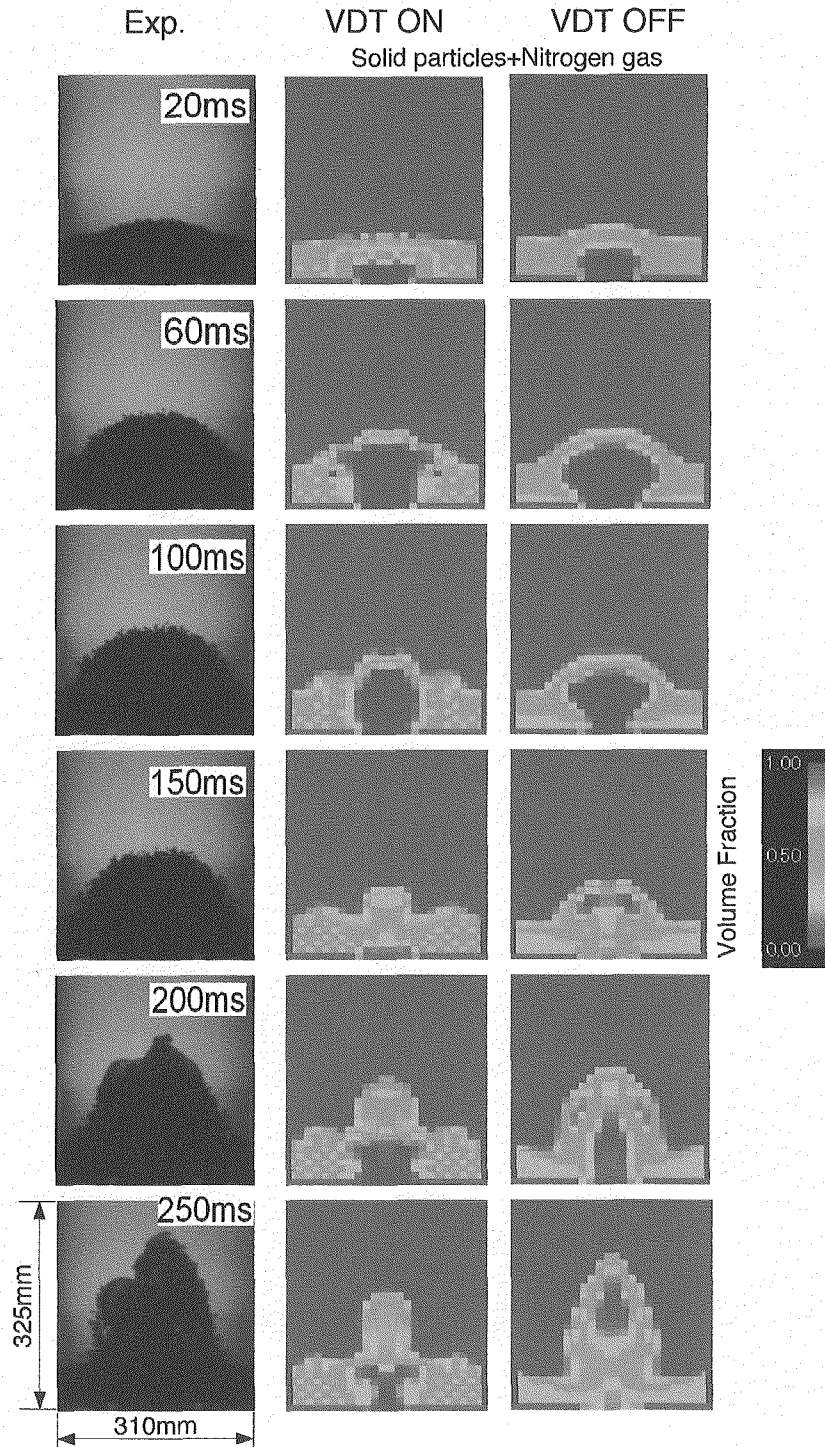
Fig. 17: Images of the particle bed for the 2nd experimental case.

The same region of a size of 310 mm (diameter of the inner cylindrical water pool) × 325 mm (height) is represented in all of the images. Images labeled "Exp.", "VDT ON", and "VDT OFF" show the experimental images, and images simulated by SIMMER-III with/without the viscous diffusion term coupled with the particle viscosity model, respectively. The initial nitrogen gas pressure is 0.296 MPa.
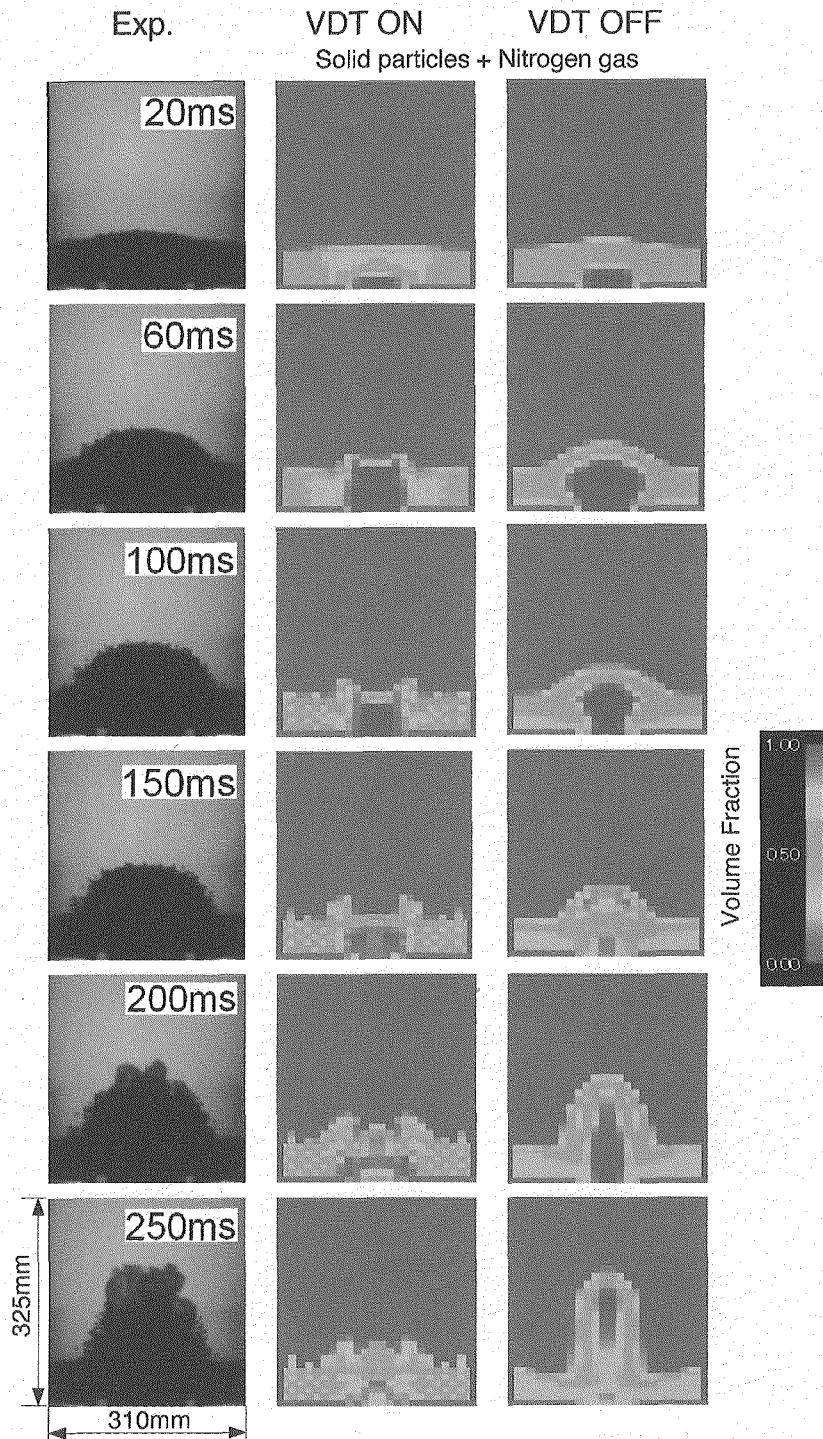
Fig. 18: Images of the particle bed for the 5th experimental case.

The same region of a size of 310 mm (diameter of the inner cylindrical water pool) × 25 mm (height) is represented in all of the images. Images labeled "Exp.", "VDT ON", and "VDT OFF" show the experimental images, and images simulated by SIMMER-III with/without the viscous diffusion term coupled with the particle viscosity model, respectively. The initial nitrogen gas pressure is 0.237 MPa.
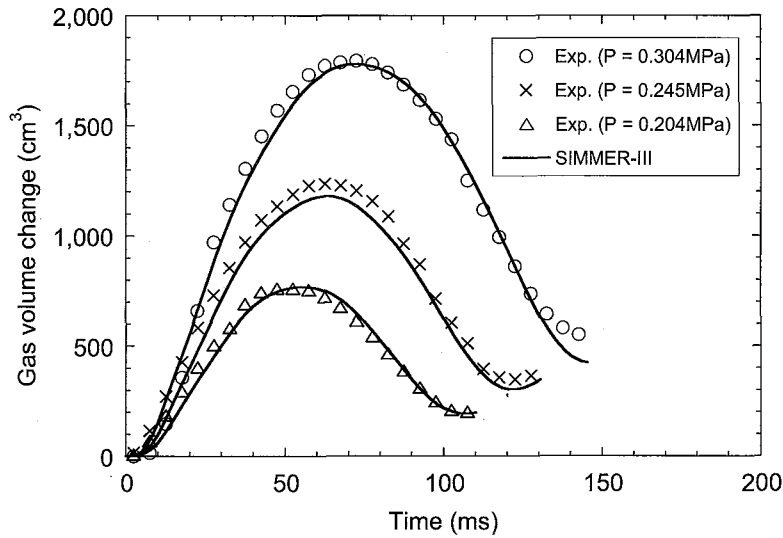
Fig. 19: Comparison of gas volume changes.

The legends "P = 0.304 MPa", "P = 0.245 MPa", and "P = 0.204 MPa", correspond to experimental cases with an initial nitrogen gas pressure of 0.304, 0.245, and 0.204 MPa, respectively. All three experimental cases employed a 50 mm height bed of YB balls.
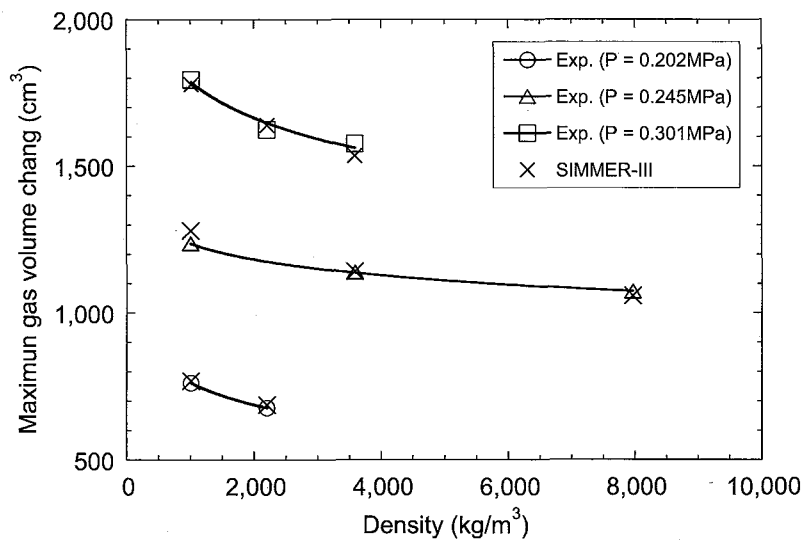
Fig. 20: Comparison of the maximum gas volume changes between cases with different particles.

The legends "P = 0.301 MPa", "P = 0.245 MPa", "P = 0.202 MPa" correspond to experimental cases with an initial nitrogen gas pressure of 0.301, 0.245, and 0.202 MPa, respectively. All these cases were based on a 50 mm height particle bed.
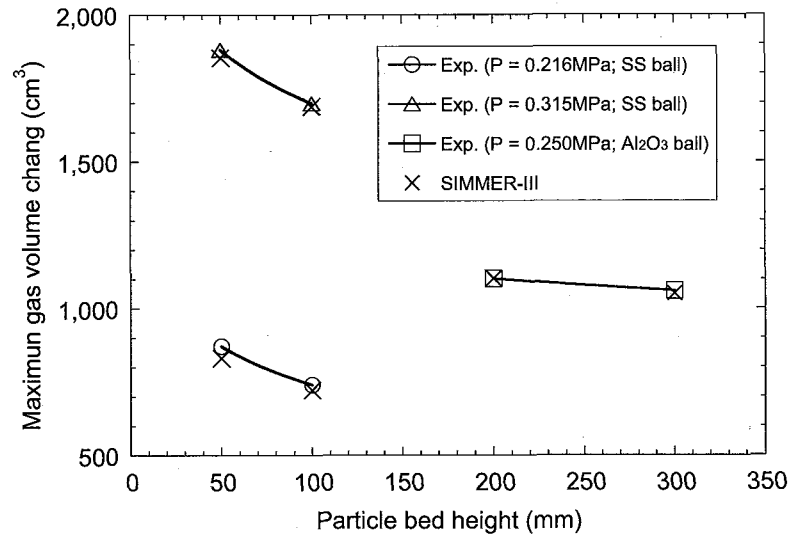
Fig. 21: Comparison of the maximum gas volume changes between cases with different bed heights.
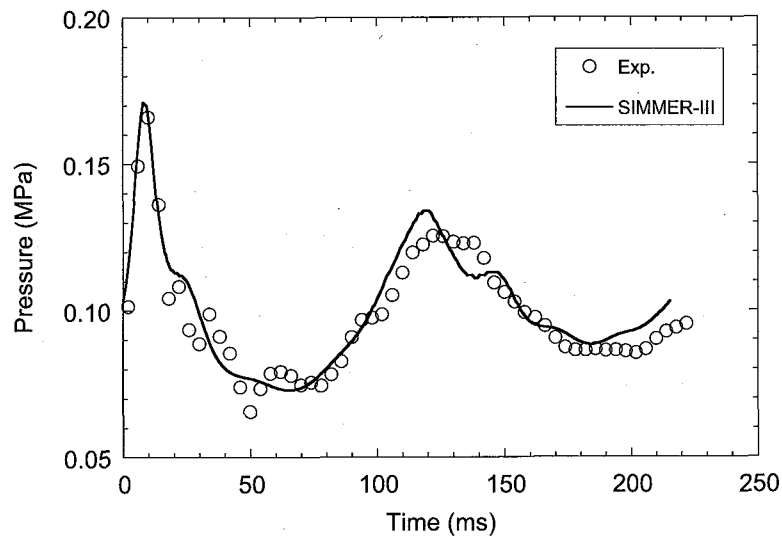
Fig. 22: Pressure transient at the top of the water pool.

The experimental case with a 100 mm height Al_2O_3 bed obtained at an initial nitrogen gas pressure of 0.246 MPa.
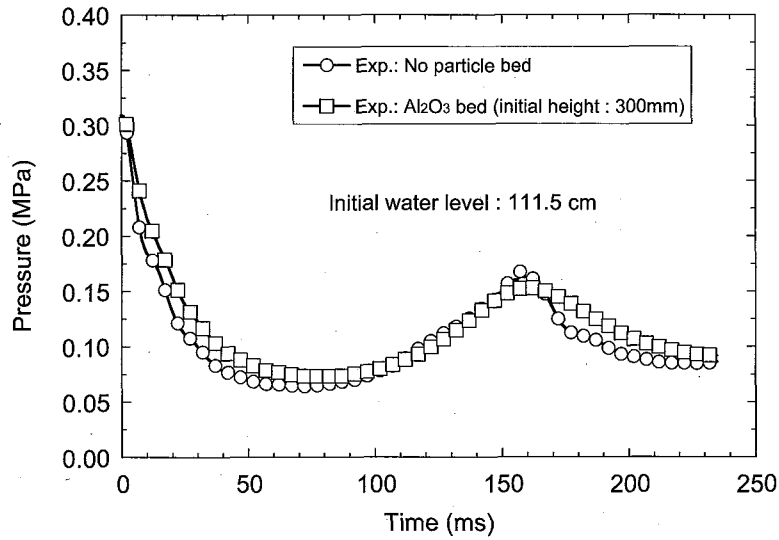
Fig. 23: Pressure transients in the pressure vessel.

Comparison of the pressure transient in the pressure vessel between the experimental cases without any particle bed and with a 300 mm height Al₂O₃ bed. Other experimental parameters were the same in both cases.
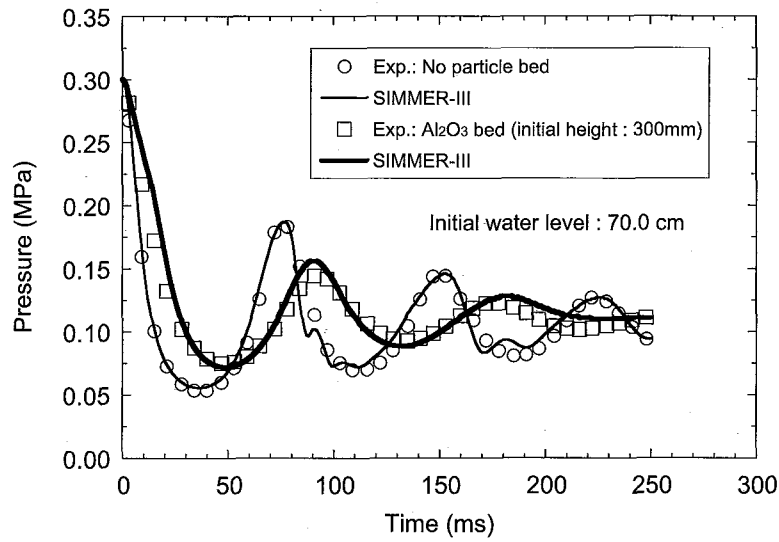
Fig. 24: Comparison of pressure transients in the pressure vessel.

Experimental cases without any particle bed (No Particle Bed) and with a 300 mm height Al₂O₃ bed (Al₂O₃ bed h = 300 mm), respectively. A lower water height in the liquid pool was used for the two experimental cases, in which the distance between the water surface and the top of the cylinder pool was 300 mm.
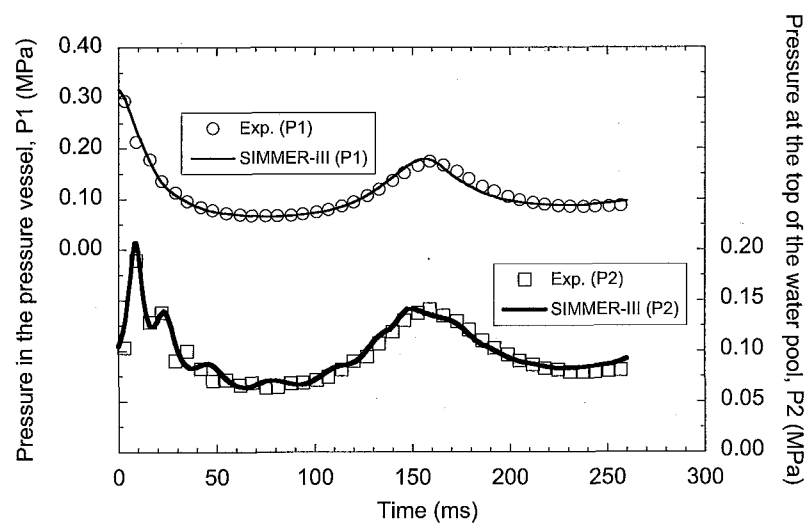
Fig. 25: Pressure transients in the case with a 50 mm height SS ball bed.

"P1" and "P2" show the pressure transients in the pressure vessel and at the top of the water pool, respectively. The initial value of "P1" is 0.318 MPa.
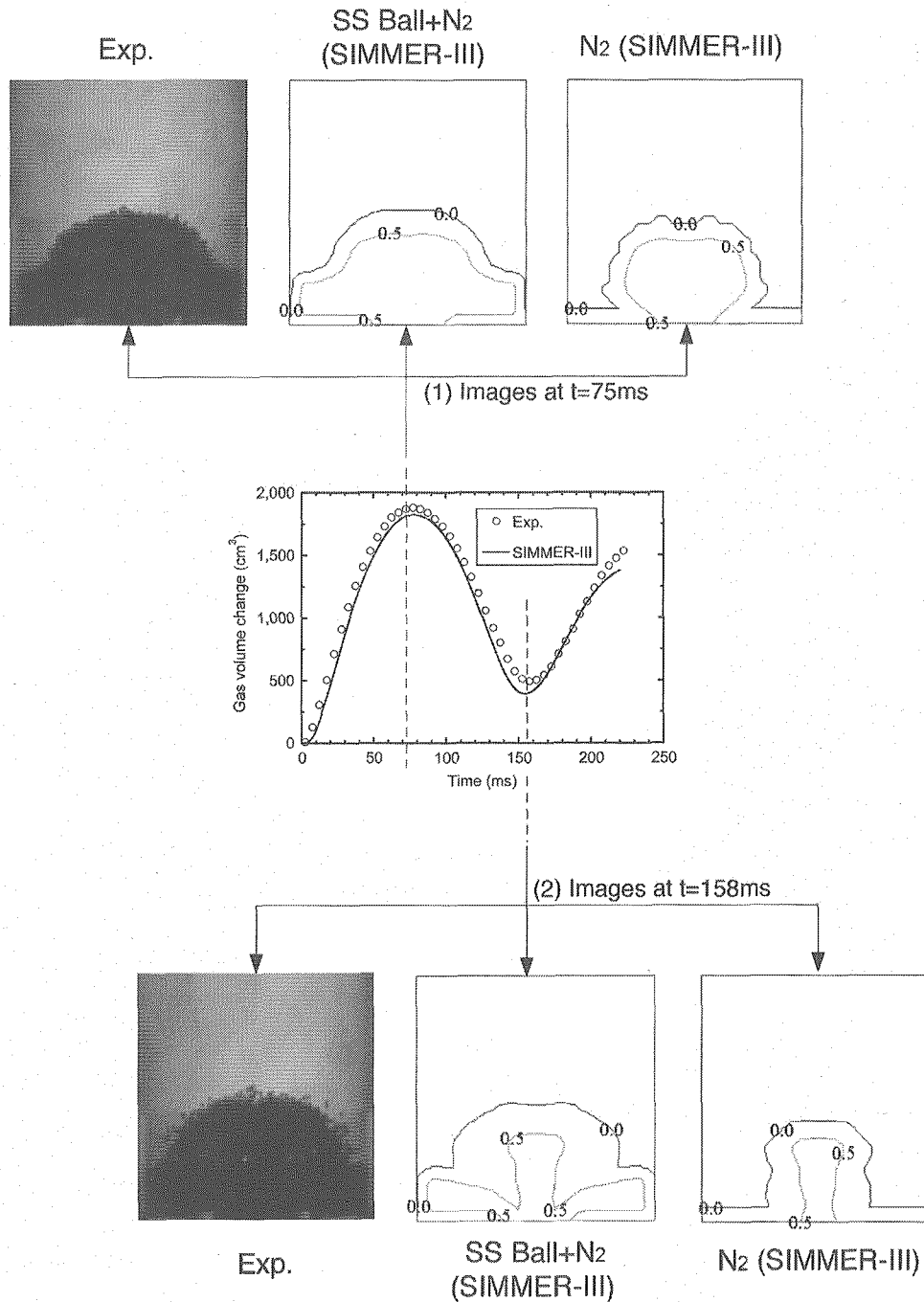
Fig. 26: Gas volume change and particle bed images in the case with a 50 mm height SS ball bed.

The initial nitrogen gas pressure was 0.318 MPa. The dimensions of the region shown in the images correspond to 310 mm (diameter of the inner cylindrical water pool) × 325 mm (height). Images labeled "Exp.", "SS Ball + N_2 (SIMMER-III)", and "N_2 (SIMMER-III)" correspond to the experimental images, the isoline images of the total volume fraction of SS balls and nitrogen gas, and the phase distribution isolines of the nitrogen gas only, respectively.
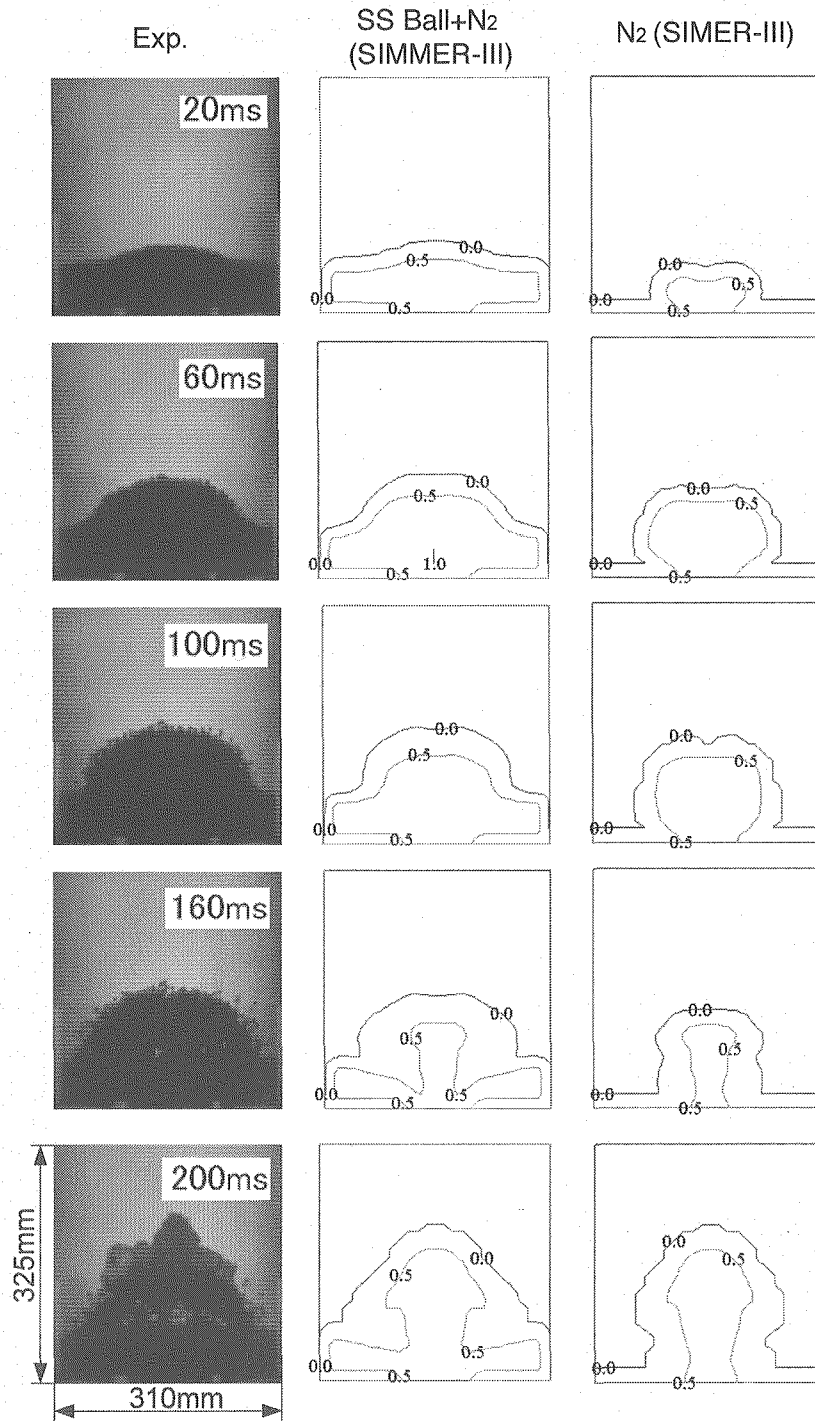
Fig. 27: Comparison of particle bed images in the case with a 50 mm height SS bed.

The initial nitrogen gas pressure was 0.318 MPa. The same region of a size of 310 mm (diameter of the inner cylindrical water pool) × 325 mm (height) is represented in all of the images. Images labeled "Exp.", "SS Ball + N_2 (SIMMER-III), and "N_2 (SIMMER-III)" show the experimental images, the isoline images of the total volume fraction of SS balls and nitrogen gas, and the phase distribution isolines of the nitrogen gas only, respectively.
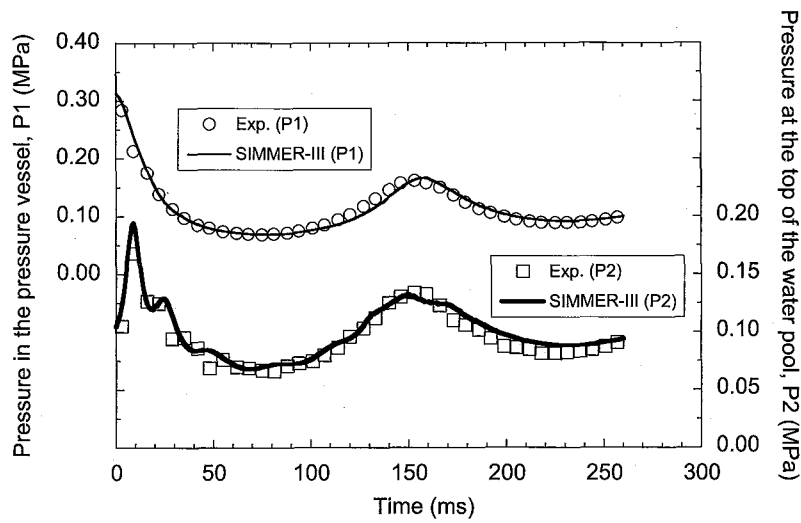
Fig. 28: Pressure transients in the case with a 100 mm height SS ball bed.

"P1" and "P2" show the pressure transients in the pressure vessel and at the top of the water pool, respectively. The initial value of "P1" is 0.313 MPa.
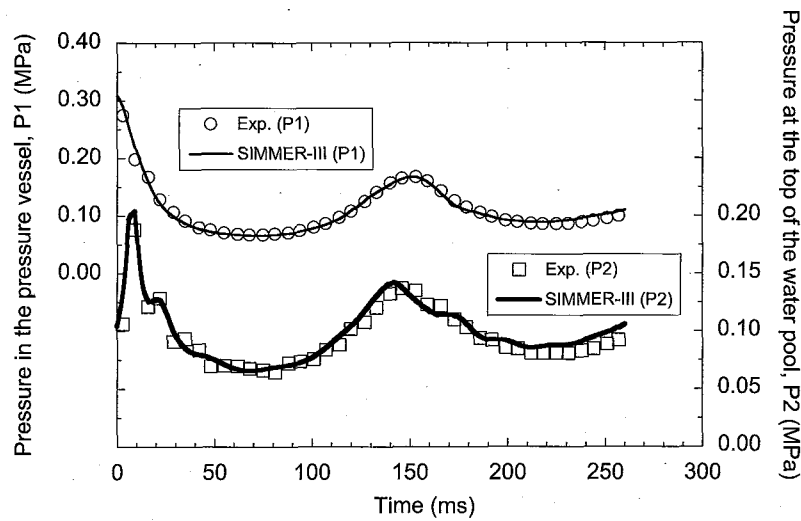
Fig. 29: Pressure transients in the case with a 100 mm height Al_2O_3 bed.

"P1" and "P2" show the pressure transients in the pressure vessel and at the top of the water pool, respectively. The initial value of "P1" is 0.308 MPa.
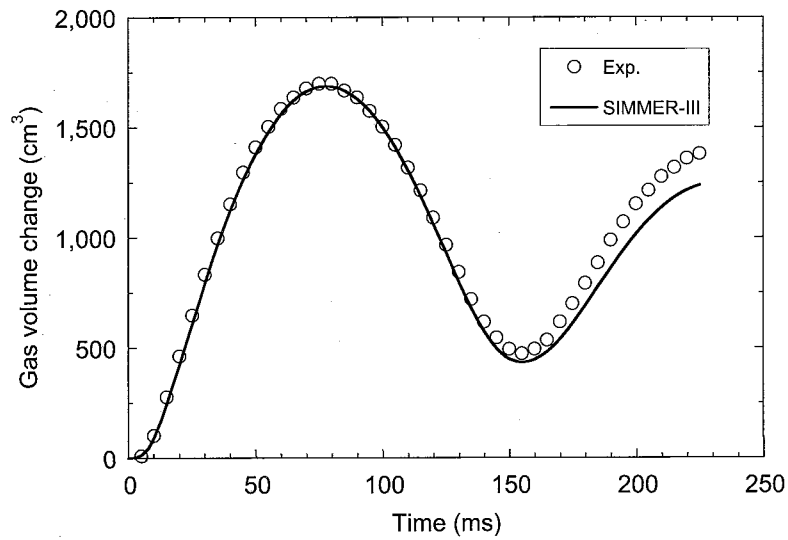
Fig. 30: Gas volume change in the case with a 100 mm height SS ball bed.

The initial nitrogen gas pressure was 0.313 MPa.
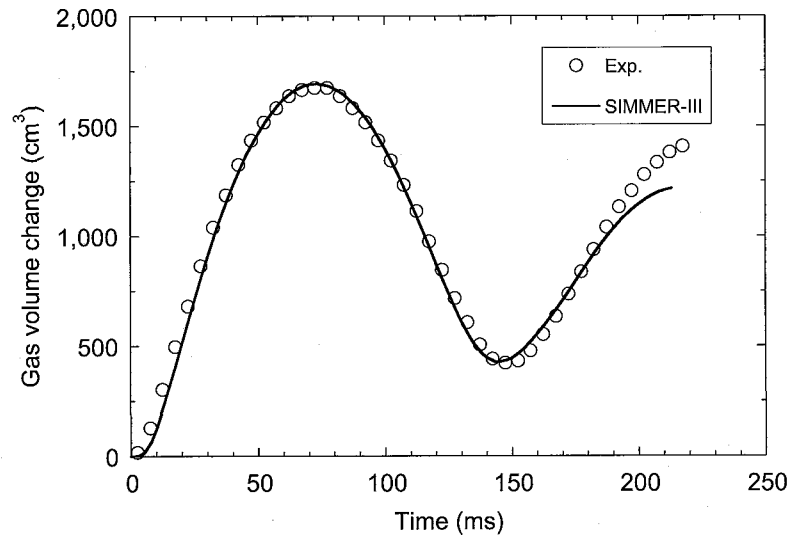
Fig. 31: Gas volume change in the case with a 100 mm height Al$_2$O$_3$ bed.

The initial nitrogen gas pressure was 0.308 MPa.
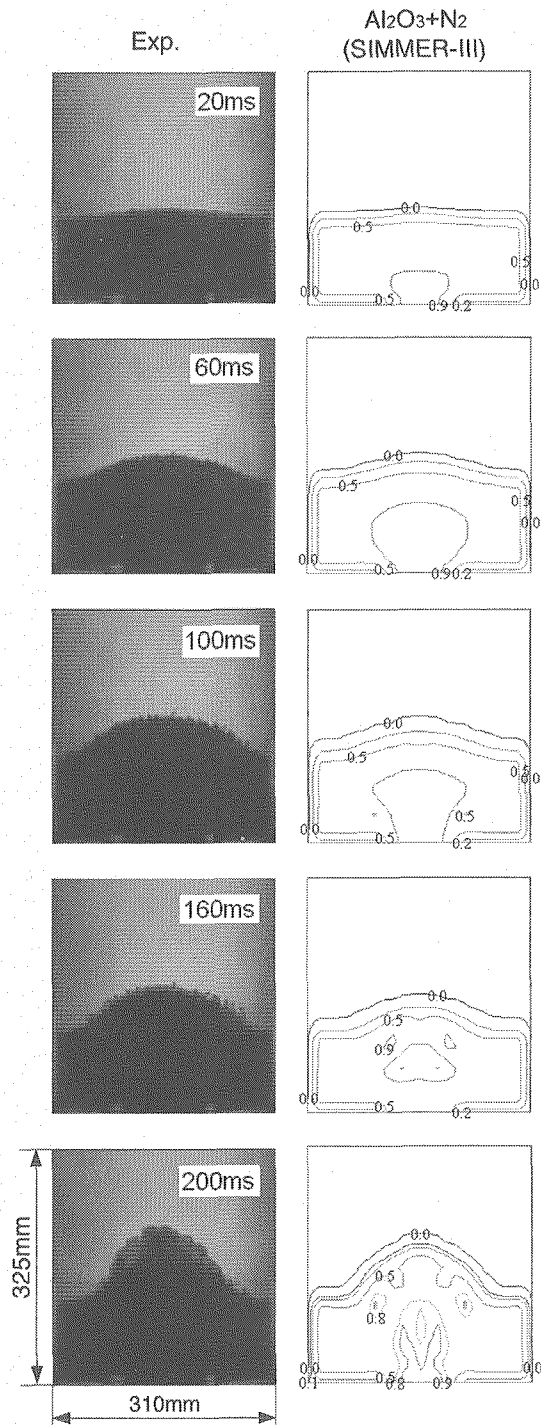
Fig. 32: Comparison of particle bed images in the case with a 100 mm height Al₂O₃ bed.

The initial nitrogen gas pressure was 0.308 MPa. The same region of a size of 310 mm (diameter of the inner cylindrical water pool) × 325 mm (height) is represented in all of the images. Images labeled "Exp." and "Al₂O₃ + N₂ (SIMMER-III)" show the experimental images, the isoline images of the total volume fraction of Al₂O₃ and nitrogen gas, respectively.
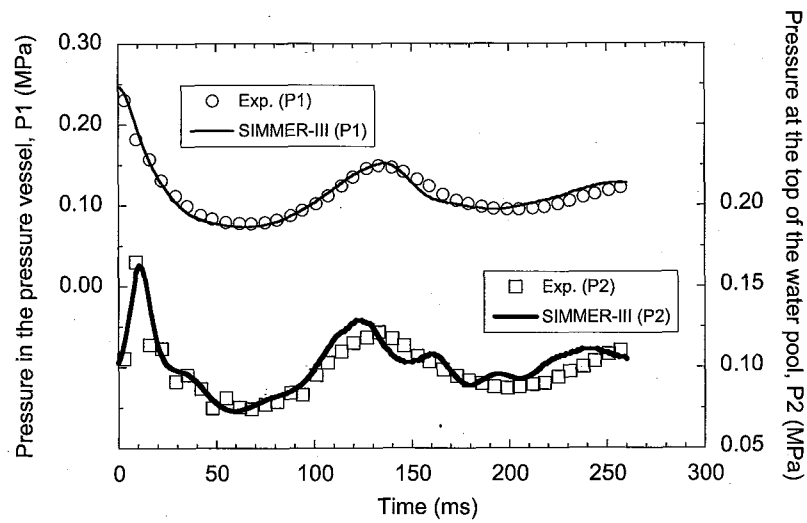
Fig. 33: Pressure transients in the case with a 200 mm height Al₂O₃ bed.

"P1" and "P2" show the pressure transients in the pressure vessel and at the top of the water pool, respectively. The initial value of "P1" is 0.248 MPa.
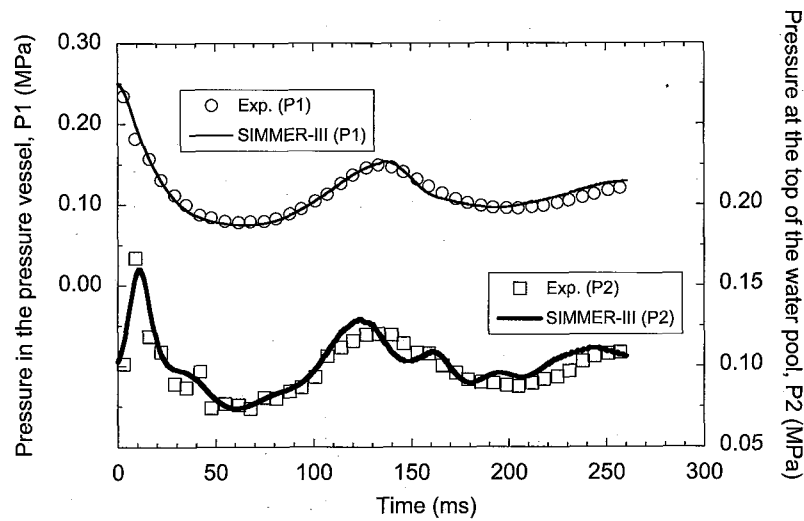
Fig. 34: Pressure transients in the case with a 300 mm height Al₂O₃ bed.

"P1" and "P2" show the pressure transients in the pressure vessel and at the top of the water pool, respectively. The initial value of "P1" is 0.251 MPa.
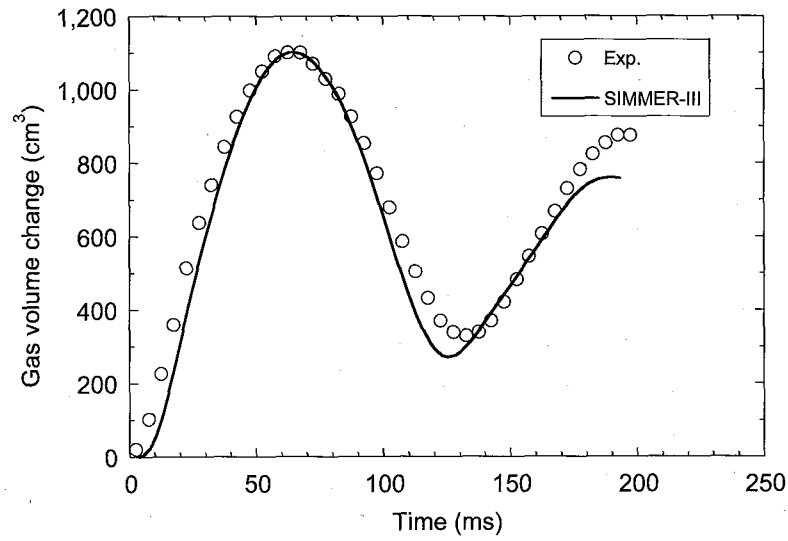
Fig. 35: Gas volume change in the case with a 200 mm height Al₂O₃ bed.

The initial nitrogen gas pressure was 0.248 MPa.
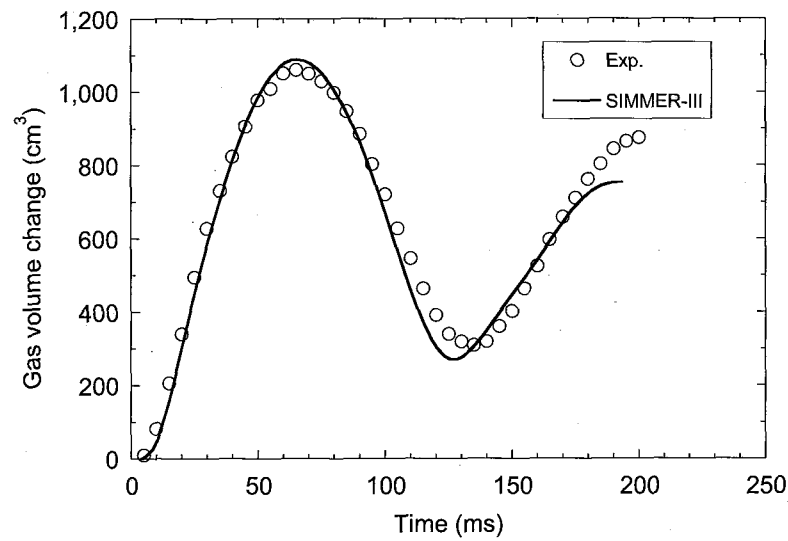
Fig. 36: Gas volume change in the case with a 300 mm height Al₂O₃ bed.

The initial nitrogen gas pressure was 0.251 MPa.

This is a blank page.

国際単位系（SI）

表1．SI 基本単位

基本量	SI 基本単位	
	名称	記号
長 さ	メートル	m
質 量	キログラム	kg
時 間	秒	s
電 流	アンペア	A
熱力学温度	ケルビン	K
物 質 量	モル	mol
光 度	カンデラ	cd

表2．基本単位を用いて表されるSI組立単位の例

組立量	SI 基本単位	
	名称	記号
面 積	平方メートル	m²
体 積	立法メートル	m³
速さ，速度	メートル毎秒	m/s
加 速 度	メートル毎秒毎秒	m/s²
波 数	毎メートル	m⁻¹
密度（質量密度）	キログラム毎立法メートル	kg/m³
質量体積（比体積）	立法メートル毎キログラム	m³/kg
電 流 密 度	アンペア毎平方メートル	A/m²
磁界の強さ	アンペア毎メートル	A/m
（物質量の）濃度	モル毎立方メートル	mol/m³
輝 度	カンデラ毎平方メートル	cd/m²
屈 折 率	（数の）1	1

表5．SI 接頭語

乗数	接頭語	記号	乗数	接頭語	記号
10²⁴	ヨタ	Y	10⁻¹	デシ	d
10²¹	ゼタ	Z	10⁻²	センチ	c
10¹⁸	エクサ	E	10⁻³	ミリ	m
10¹⁵	ペタ	P	10⁻⁶	マイクロ	μ
10¹²	テラ	T	10⁻⁹	ナノ	n
10⁹	ギガ	G	10⁻¹²	ピコ	p
10⁶	メガ	M	10⁻¹⁵	フェムト	f
10³	キロ	k	10⁻¹⁸	アト	a
10²	ヘクト	h	10⁻²¹	ゼプト	z
10¹	デカ	da	10⁻²⁴	ヨクト	y

表3．固有の名称とその独自の記号で表されるSI組立単位

組立量	SI 組立単位			
	名称	記号	他のSI単位による表し方	SI基本単位による表し方
平 面 角	ラジアン [a]	rad		m·m⁻¹=1 [b]
立 体 角	ステラジアン [a]	sr [c]		m²·m⁻²=1 [b]
周 波 数	ヘルツ	Hz		s⁻¹
力	ニュートン	N		m·kg·s⁻²
圧力，応力	パスカル	Pa	N/m²	m⁻¹·kg·s⁻²
エネルギー，仕事，熱量	ジュール	J	N・m	m²·kg·s⁻²
工率，放射束	ワット	W	J/s	m²·kg·s⁻³
電荷，電気量	クーロン	C		s·A
電位差（電圧），起電力	ボルト	V	W/A	m²·kg·s⁻³·A⁻¹
静 電 容 量	ファラド	F	C/V	m⁻²·kg⁻¹·s⁴·A²
電 気 抵 抗	オーム	Ω	V/A	m²·kg·s⁻³·A⁻²
コンダクタンス	ジーメンス	S	A/V	m⁻²·kg⁻¹·s³·A²
磁 束	ウェーバ	Wb	V・s	m²·kg·s⁻²·A⁻¹
磁 束 密 度	テスラ	T	Wb/m²	kg·s⁻²·A⁻¹
インダクタンス	ヘンリー	H	Wb/A	m²·kg·s⁻²·A⁻²
セルシウス温度	セルシウス度 [d]	℃		K
光 束	ルーメン	lm	cd·sr [c]	m²·m⁻²·cd=cd
照 度	ルクス	lx	lm/m²	m²·m⁻⁴·cd=m⁻²·cd
（放射性核種の）放射能	ベクレル	Bq		s⁻¹
吸収線量，質量エネルギー分与，カーマ	グレイ	Gy	J/kg	m²·s⁻²
線量当量，周辺線量当量，方向性線量当量，個人線量当量，組織線量当	シーベルト	Sv	J/kg	m²·s⁻²

(a)ラジアン及びステラジアンの使用は、同じ次元であっても異なった性質をもった量を区別するときの組立単位の表し方として利点がある。組立単位を形作るときのいくつかの用例は表4に示されている。

(b)実際には、使用する時には記号rad及びsrが用いられるが、習慣として組立単位としての記号"1"は明示されない。

(c)測光学では、ステラジアンの名称と記号srを単位の表し方の中にそのまま維持している。

(d)この単位は、例としてミリセルシウス度m℃のようにSI接頭語を伴って用いても良い。

表6．国際単位系と併用されるが国際単位系に属さない単位

名称	記号	SI 単位による値
分	min	1 min=60s
時	h	1h =60 min=3600 s
日	d	1 d=24 h=86400 s
度	°	1° =(π/180) rad
分	′	1′ =(1/60)° =(π/10800) rad
秒	″	1″ =(1/60)′ =(π/648000) rad
リットル	l，L	1l=1 dm³=10⁻³m³
トン	t	1t=10³ kg
ネーパ	Np	1Np=1
ベル	B	1B=(1/2)ln10（Np）

表7．国際単位系と併用されこれに属さない単位で SI単位で表される数値が実験的に得られるもの

名称	記号	SI 単位であらわされる数値
電子ボルト	eV	1eV=1.60217733(49)×10⁻¹⁹J
統一原子質量単位	u	1u=1.6605402(10)×10⁻²⁷kg
天 文 単 位	ua	1ua=1.49597870691(30)×10¹¹m

表8．国際単位系に属さないが国際単位系と併用されるその他の単位

名称	記号	SI 単位であらわされる数値
海 里		1 海里=1852m
ノット		1 ノット=1 海里毎時=(1852/3600)m/s
アール	a	1a=1 dam²=10²m²
ヘクタール	ha	1 ha=1 hm²=10⁴m²
バール	bar	1 bar=0.1MPa=100kPa=1000hPa=10⁵Pa
オングストローム	Å	1 Å=0.1nm=10⁻¹⁰m
バーン	b	1 b=100fm²=10⁻²⁸m²

表4．単位の中に固有の名称とその独自の記号を含むSI組立単位の例

組立量	SI 組立単位		
	名称	記号	SI 基本単位による表し方
粘 度	パスカル秒	Pa·s	m⁻¹·kg·s⁻¹
力のモーメント	ニュートンメートル	N・m	m²·kg·s⁻²
表 面 張 力	ニュートン毎メートル	N/m	kg·s⁻²
角 速 度	ラジアン毎秒	rad/s	m·m⁻¹·s⁻¹=s⁻¹
角 加 速 度	ラジアン毎平方秒	rad/s²	m·m⁻¹·s⁻²=s⁻²
熱流密度，放射照度	ワット毎平方メートル	W/m²	kg·s⁻³
熱容量，エントロピー	ジュール毎ケルビン	J/K	m²·kg·s⁻²·K⁻¹
質量熱容量（比熱容量），質量エントロピー	ジュール毎キログラム毎ケルビン	J/(kg·K)	m²·s⁻²·K⁻¹
質量エネルギー（比エネルギー）	ジュール毎キログラム	J/kg	m²·s⁻²·K⁻¹
熱 伝 導 率	ワット毎メートル毎ケルビン	W/(m·K)	m·kg·s⁻³·K⁻¹
体積エネルギー	ジュール毎立方メートル	J/m³	m⁻¹·kg·s⁻²
電界の強さ	ボルト毎メートル	V/m	m·kg·s⁻³·A⁻¹
体 積 電 荷	クーロン毎立方メートル	C/m³	m⁻³·s·A
電 気 変 位	クーロン毎平方メートル	C/m²	m⁻²·s·A
誘 電 率	ファラド毎メートル	F/m	m⁻³·kg⁻¹·s⁴·A²
透 磁 率	ヘンリー毎メートル	H/m	m·kg·s⁻²·A⁻²
モルエネルギー	ジュール毎モル	J/mol	m²·kg·s⁻²·mol⁻¹
モルエントロピー，モル熱容量	ジュール毎モル毎ケルビン	J/(mol·K)	m²·kg·s⁻²·K⁻¹·mol⁻¹
照射線量（X線及びγ線）	クーロン毎キログラム	C/kg	kg⁻¹·s·A
吸 収 線 量 率	グレイ毎秒	Gy/s	m²·s⁻³
放 射 強 度	ワット毎ステラジアン	W/sr	m⁴·m⁻²·kg·s⁻³=m²·kg·s⁻³
放 射 輝 度	ワット毎平方メートル毎ステラジアン	W/(m²·sr)	m²·m⁻²·kg·s⁻³=kg·s⁻³

表9．固有の名称を含むCGS組立単位

名称	記号	SI 単位であらわされる数値
エ ル グ	erg	1 erg=10⁻⁷ J
ダ イ ン	dyn	1 dyn=10⁻⁵N
ポ ア ズ	P	1 P=1 dyn·s/cm²=0.1Pa·s
ストークス	St	1 St =1cm²/s=10⁻⁴m²/s
ガ ウ ス	G	1 G ^10⁻⁴T
エルステッド	Oe	1 Oe ^(1000/4π)A/m
マクスウェル	Mx	1 Mx ^10⁻⁸Wb
スチルブ	sb	1 sb =1cd/cm²=10⁴cd/m²
ホト	ph	1 ph=10⁴lx
ガ ル	Gal	1 Gal =1cm/s²=10⁻²m/s²

表10．国際単位に属さないその他の単位の例

名称	記号	SI 単位であらわされる数値
キュリー	Ci	1 Ci=3.7×10¹⁰Bq
レントゲン	R	1 R = 2.58×10⁻⁴C/kg
ラ ド	rad	1 rad=1cGy=10⁻²Gy
レ ム	rem	1 rem=1 cSv=10⁻²Sv
X 線 単 位		1X unit=1.002×10⁻⁴nm
ガ ン マ	γ	1 γ =1 nT=10⁻⁹T
ジャンスキー	Jy	1 Jy=10⁻²⁶W·m⁻²·Hz⁻¹
フ ェ ル ミ		1 fermi=1 fm=10⁻¹⁵m
メートル系カラット		1 metric carat = 200 mg = 2×10⁻⁴kg
ト ル	Torr	1 Torr = (101 325/760) Pa
標 準 大 気 圧	atm	1 atm = 101 325 Pa
カ ロ リ ー	cal	
ミ ク ロ ン	μ	1 μ =1μm=10⁻⁶m